Solution Property Preserving Reconstruction BVD+MOOD Scheme for Compressible Euler Equations with Source Terms and Detonations

Siengdy Tann, Xi Deng, Raphaël Loubère, Feng Xiao

Solution Property Preserving Reconstruction BVD+MOOD Scheme for Compressible Euler Equations with Source Terms and Detonations

Siengdy Tann[*,a]

Xi Deng[b], Raphaël Loubère[c,*], Feng Xiao[*,a]

[a] *Department of Mechanical Engineering, Tokyo Institute of Technology, 2-12-1 Ookayama, Meguro-ku, Tokyo, 152-8550, Japan*
[b] *Department of Aeronautics, Imperial College London, SW7 2AZ, United Kingdom*
[c] *Institut de Mathématiques de Bordeaux (IMB), Université de Bordeaux, CNRS, Bordeaux INP, F33400, Talence, France*

Abstract

In "Solution Property Reconstruction for Finite Volume scheme: a BVD+MOOD framework", Int. J. Numer. Methods Fluids, 2020, we have designed a novel solution property preserving reconstruction, so-called multi-stage BVD-MOOD scheme. The scheme is able to maintain a high accuracy in smooth profile, eliminate the oscillations in the vicinity of discontinuity, capture sharply discontinuity and preserve some physical properties like the positivity of density and pressure for the Euler equations of compressible gas dynamics. In this paper, we present an extension of this approach for the compressible Euler equations supplemented with source terms (e.g., gravity, chemical reaction). One of the main challenges when simulating these models is the occurrence of negative density or pressure during the time evolution, which leads to a blow-up of the computation. General compressible Euler equations with different type of source terms are considered as models for physical situations such as detonation waves. Then, we illustrate the performance of the proposed scheme via a numerical test suite including genuinely demanding numerical tests. We observe that the present scheme is able to preserve the physical properties of the numerical solution still ensuring robustness and accuracy when and where appropriate.

Key words: Finite volume, multi-stage BVD, THINC, positivity-preserving, MOOD, source

[*]Corresponding author:
Email addresses: `tann.s.aa@m.titech.ac.jp` (Siengdy Tann), `raphael.loubere@u-bordeaux.fr` (Raphaël Loubère), `xiao.f.aa@m.titech.ac.jp` (Feng Xiao)

terms

---

1. Introduction

The finite volume method has been developed and employed to solve CFD problems in wide range of applications for many decades. The first order finite volume method, known as Godunov scheme [29, 59], possesses interesting properties such as conservativeness, monotonicity, positivity-preserving and extreme robustness. Nonetheless, it generates excessive numerical dissipation and tends to smear out the flow structures. In order to reduce the numerical dissipation and to capture shocks exempt from spurious oscillation, high-resolution conservative schemes have been developed over the last half century. A class of non-linear schemes can effectively eliminate numerical oscillations by introducing flux or slope limiters, for instance, Flux Corrected Transport (FCT) scheme [5, 71], Total Variation Diminishing (TVD) scheme [31, 54], and Monotone Upstream-centered Scheme for Conservative Laws (MUSCL) [40, 41], which reach a nominal 2nd order accuracy, but still suffer from important numerical dissipation with a tendency to smear out flow structures, such as vortices and contact discontinuities. Consecutively, methods using reconstructions of higher order polynomials for smooth solutions, such as in the Piecewise Parabolic Method (PPM) [13, 33], Essential Non-oscillatory (ENO) scheme [49, 50], Weighted Essential Non-oscillatory (WENO) schemes [34, 46, 25, 1], have been proposed to achieve higher order of accuracy, and, suppress the spurious numerical oscillations by limiting procedures based on smoothness indicators. Nevertheless, high order schemes with conventional limiting procedure may still generate non-physical fluid properties such as negative density or pressure, which lead to blow-up of the computation and subsequent code crash. Most of high order schemes fail to preserve positivity because of interpolation errors when near vacuum states occur or in the presence of strong shocks. Recently, some positivity-preserving techniques for high order schemes were developed by Zhang and Shu as in [73, 74, 76, 45, 69] for homogeneous compressible Euler equations, and, in [75, 62, 77] for compressible Euler equations with several types of source terms, like the energetic reactive products in gaseous detonations for example.

A new guideline for high-resolution schemes, see [53, 17], was designed to capture shocks with low numerical dissipation: the so-called Boundary Variation Diminishing (BVD) method under the finite volume framework. A hybrid reconstruction scheme [53] coupling WENO and THINC (Tangent of Hyperbola for INterface Capturing) reconstructions is employed using the BVD algorithm which automatically selects the appropriate reconstruction. For instance, THINC method [66, 67, 51], originally devised as a volume of fluid (VOF) scheme, reconstructs appropriately jump-like solution and is then employed to capture the discontinuous solutions. As the result, the BVD algorithm is capable to resolve both smooth and discontinuous profiles with high-fidelity, see [53, 17, 14]. Furthermore, new limiter-free BVD strategies have been proposed [15, 16] by introducing multi-stages. These so-called $\mathrm{P_nT_m}$-BVD methods employ unlimited high order polynomials and THINC reconstructions. $\mathrm{P_nT_m}$-BVD stands for unlimited polynomial of nth degree and THINC function of mth level reconstruction relies on BVD algorithm. According to numerical experiments in [15], the $\mathrm{P_nT_m}$-BVD schemes can achieve very high order accuracy (up to 11th order) for smooth solution, and sharply capture discontinuous solution without spurious numerical oscillations.

Different from classical *a priori* limiting schemes, the Multi-dimensional Optimal Order Detection (MOOD), also known as *a posteriori* limiting scheme, was proposed in [10, 19, 21], and has been employed in various numerical formulations [7, 20, 6] and applications [11, 22, 8, 36, 4, 24, 61, 56] and more recently [23, 57, 27]. In MOOD algorithm, some criterions or detectors were designed based on the computational stability and physical properties. The MOOD algorithm is performed after computing a candidate solution, *i.e.* a solution at the next time level, then MOOD split the cells into valid/accepted/good and invalid/troubled/bad ones. For a valid cell, the criteria of physical admissible detection (PAD) and numerical admissible detection (NAD) are both satisfied, the candidate solution is then accepted for next time step. Otherwise, if a cell does not satisfy the criterion, the solution in this cell is recomputed by decrementing the degree of the local reconstructed polynomial. This process continues and stops when the cell is detected as valid or when the lowest possible polynomial degree is reached (piecewise constant, that is no-reconstruction).

In this paper, we extend the novel high-fidelity positivity-preserving numerical scheme proposed in [55] for the perfect gas Euler equations with source terms. For instance, we couple the BVD and MOOD techniques to get and maintain the high order accuracy, a shock capturing and positivity preserving property. For the BVD strategy, the candidate reconstructions are: the linear 4th degree polynomial (P4) for smooth solutions, and THINC functions to get an oscillation-free and sharp shock capturing scheme. In addition, a MOOD method detects the obtained candidate solution at the next time level by the physical admissible detection (PAD). The multi-stage BVD-MOOD scheme is able to resolve smooth solutions, effectively eliminate spurious oscillations, sharply capture discontinuous solutions, and, preserve the positivity. In the present work, we simulate several demanding numerical tests for compressible Euler equations with various source terms modelling gravity or detonation waves.

This paper is organized as follows. In Section 2, we briefly introduce the numerical methods as well as the general finite volume method. We present in Section 3 the details of solution property preserving reconstruction ensuring high-order accuracy (HO), essentially non-oscillatory (ENO) behaviour, sharp capture of discontinuities and robustness for extreme situations. We then extend the numerical scheme into two-dimensions in Section 4. In the numerical Section 5, we present the results on some benchmark tests for homogeneous Euler equations and then with various source terms. This will testify that the present scheme is able to capture both smooth and discontinuous solutions and preserve their physical validity for various problems with source terms. We end the paper with a brief summary and future plans in Section 6.

2. Numerical Methods for one dimensional space

2.1. Governing Equations

We consider the general form of one dimensional Euler equations with source terms, which is defined as

$$\frac{\partial U}{\partial t} + \frac{\partial F(U)}{\partial x} = S(U); \quad t \geq 0, \quad x \in \mathbb{R} \tag{1}$$

where $U(x,t) = (\rho, \rho u, E)^T$, $F(U) = [\rho u, \rho u^2 + p, (E+p)u]^T$ and ρ, u, p are the density, velocity and pressure, respectively. E is the total energy expressed as $E = e + \frac{1}{2}\rho u^2$ and e is the internal energy, they are linked to the pressure through an equation of state (EOS) $p \equiv p(\rho, e)$ from which we can define the sound speed $a > 0$. The homogeneous system is the hyperbolic hydrodynamics system of conservation laws. In this paper, we consider two types of source terms $S(U)$, *i.e.* gravity acceleration and detonation models of premixed reactive gases, which are detailed later.

The source terms are possibly becoming stiff compared to the local time and space scales, and usually their main effect is to drastically modify the behavior of the solution.

2.2. Operator splitting

To solve the above model system, the numerical solution at each time step interval $[t, t+\Delta t]$ is computed in a split way: First the homogeneous conservation law (convection step) and, second the ODE system (source term step or reaction step). We describe in the following the fractional step approach [59] for gravity source terms, and, the second order Strang-splitting method [52] for the more complex chemical reaction source terms.

The Euler equations with gravity-like source terms. The numerical solution at time level $t + \Delta t$ is approximated by

$$U(t + \Delta t) = C(\Delta t)\, R(\Delta t)\, U(t). \tag{2}$$

The convection operator $C(\Delta t)$ approximates the solution on the time interval $U(t + \Delta t)$ from the approximate solution $U(t)$, solving

$$\frac{\partial U}{\partial t} + \frac{\partial F(U)}{\partial x} = 0, \quad t \leq t' \leq t + \Delta t. \tag{3}$$

Different numerical schemes for hyperbolic conservation laws can be used at this stage. In this paper, we use the third-order TVD Runge-Kutta method [30] for time integration and the multi-stage BVD-MOOD scheme for spatial discretization [55] supplemented with HLLCM Riemann solver [48] to prevent the carbuncle phenomenon or shock instability. Other approximate Riemann solvers could be also employed for most cases.

The source term operator $R(\Delta t)$ approximates the solution on a time step of the ODE system

$$\frac{dU}{dt} = S(U), \quad t \leq t' \leq t + \Delta t. \tag{4}$$

Any ODE solver can be used to deal with such source terms.

The reactive Euler equations. The numerical solution at time level $t + \Delta t$ is approximated generically by

$$U(t + \Delta t) = C\left(\frac{\Delta t}{2}\right) R\left(\frac{\Delta t}{N_r}\right) \cdots R\left(\frac{\Delta t}{N_r}\right) C\left(\frac{\Delta t}{2}\right) U(t) \tag{5}$$

Similarly, C is the convection operator acting over time $\Delta t/2$ and R is the reaction operator acting for N_r successive sub-steps. We use $N_r = 2$ sub-steps in this work. Any ODE solver can be used for the reaction operator providing that the discontinuities are sharply dealt with during the convective step.

2.3. Finite Volume Method

In this section, we briefly describe the fundamental algorithm under the finite volume context for the convection step. Let us consider the computational domain in space as $\Omega = [x^L, x^R]$ divided into N non-overlapping cells with $I_i = [x_{i-1/2}, x_{i+1/2}]$, for $i = 1, 2, ..., N$. The cell size is denoted by $\Delta x = x_{i+1/2} - x_{i-1/2}$ and is uniform over the computation domain. Furthermore, the time variable is denoted by t and $0 < t < t_{\text{final}}$, where $t_{\text{final}} > 0$ is the terminal time for the computation. The time is split into N_t non-uniform time steps paving the interval $[0, t_{\text{final}}]$. The time step is denoted as $\Delta t = t^{n+1} - t^n > 0$, where t^n is the time at n^{th} step, likewise for t^{n+1}. The time-step will be restricted by a CFL condition later.

We employ the volume integrated-average (VIA) of the solution $U(x,t)$ using a standard finite volume semi-discretization, over a mesh cell I_i at time t as

$$U_i(t) = \frac{1}{\Delta x} \int\limits_{x_{i-1/2}}^{x_{i+1/2}} U(x,t)\, dx \qquad \text{where} \qquad i = 1, 2, \ldots, N. \tag{6}$$

The VIA $U_i(t)$ for each cell I_i is updated by

$$\frac{dU_i(t)}{dt} = -\frac{1}{\Delta x} \left(F_{i+1/2}(t) - F_{i-1/2}(t) \right), \tag{7}$$

where $F_{i+1/2}(t)$ and $F_{i-1/2}(t)$ are the numerical fluxes at cell boundaries, calculated by a (approximated) Riemann solver

$$F_{i+1/2}(t) = F^{\text{Riemann}}_{i+1/2}(U^L_{i+1/2}, U^R_{i+1/2}, t), \tag{8}$$

where $U^L_{i+1/2}$ and $U^R_{i+1/2}$ are the left-side and right-side values of U at $x_{i+1/2}$ respectively. They are computed by a so-called reconstruction procedure over left and right potential stencils. The approximate flux in (9) can be written for a wide range of Riemann solvers into the general form

$$F^{\text{Riemann}}_{i+1/2}(U^L_{i+1/2}, U^R_{i+1/2}, t) = \frac{1}{2} \left(F(U^L_{i+1/2}) + F(U^R_{i+1/2}) \right) - \frac{|a_{i+1/2}|}{2} (U^R_{i+1/2} - U^L_{i+1/2}) \tag{9}$$

where $a_{i+1/2}$ varies among different Riemann solvers. As already mentioned we use the HLLCM approximate Riemann solver, the details of which can be found in [48].

2.4. Time Integration

In order to achieve high-order numerical accuracy in time, the discretization in time is made by the third-order TVD Runge-Kutta method (RK3, see [49, 30]). More precisely, defining

$$L(U) = -\frac{1}{\Delta x}\left(F_{i+1/2}(t) - F_{i-1/2}(t)\right), \tag{10}$$

as the spatial operator, then the time integration corresponds to a convex combination of three explicit steps as

$$\begin{aligned} &U^{(1)} = U^n + \Delta t L(U^n), \qquad U^{(2)} = \frac{3}{4}U^n + \frac{1}{4}U^{(1)} + \frac{1}{4}\Delta t L(U^{(1)}), \\ &U^{n+1} = \frac{1}{3}U^n + \frac{2}{3}U^{(2)} + \frac{2}{3}\Delta t L(U^{(2)}). \end{aligned} \tag{11}$$

This time integration scheme is restricted by the CFL condition

$$\Delta t \leq \mathrm{CFL}\frac{\Delta x}{\max_i(|u_i|, |u_i \pm a_i|)}, \tag{12}$$

where CFL < 1 is a safety constant.

The remaining main task (detailed in the next section) is the calculation of states $U^L_{i+1/2}$ and $U^R_{i+1/2}$ at given time t through a reconstruction procedure. In this work, we introduce a blending of high/low order polynomial and hyperbolic tangent reconstructions. The blending serves the purpose of preserving some of the properties of the solution. Moreover, the reconstructions are performed on the characteristics variables and each variable of the same cell employs the same reconstruction type. Because we employ high order polynomials and non-linear hyperbolic tangent as reconstruction types, the limiting procedure, mandatory to avoid Gibbs phenomenon and damp spurious oscillations, is handled in a non-classical way. Indeed following [55] we split the numerical solution into three parts: a large part of the domain welcomes a smooth solution, relatively small area suffer from the presence of discontinuous solutions, and, extremely small area present extreme physical situations (close to vacuum states for instance).

3. Reconstruction schemes for Solution Property Preserving

The numerical solution for the hyperbolic system of partial differential equations (PDEs) is split into three regions: 'smooth' (large), 'discontinuous' (few) and 'demanding' enduring physics violation (almost zero). An unlimited piece-wise high order polynomial reconstruction is employed for the smooth profile, while a shock-capturing THINC reconstruction deals with discontinuous profiles in a sharp and essentially non-oscillatory manner. At last, the demanding regions in the flow where non-admissible physical state may be computed are dealt with the monotonic, dissipative and robust first order Godunov scheme.

The numerical scheme should preserve some properties of the numerical solution related to those regions, for instance, a high accurate description of smooth profiles, an essentially non-oscillatory behavior in the vicinity of steep gradients, a sharp capture of discontinuity (contact, material interface), and, robustness for extreme situations. In order to fulfill these properties, we design a chain of different reconstruction operators via a multi-stage BVD-MOOD algorithm [55]. We denote them as $\mathcal{R}_{HO}$, $\mathcal{R}_{ENO}$, $\mathcal{R}_{SHARP}$ and $\mathcal{R}_{LO}$ standing for High Order polynomial, Essentially Non-Oscillatory, Sharp and Low Order polynomial reconstructions, respectively. The main tool is the so-called BVD which acts as a selector which chooses the most suitable reconstruction. For instance, for a smooth profile, the selector should choose the high-order reconstruction $\mathcal{R}_{HO}$, while the sharp one $\mathcal{R}_{SHARP}$ should be selected for the steep gradient or step-like profile/shock.

In this work, the BVD 'selector' is operating on two reconstructed candidates in the same cell, and, chooses the most suitable one. Since we consider of three possible reconstructions, $\mathcal{R}_{HO}$, $\mathcal{R}_{ENO}$ or $\mathcal{R}_{SHARP}$, then the BVD algorithm acts in 2 stages leading to a so-called multi-stage BVD, see figure 1. This BVD algorithm is exhaustively described in section 3.4.

3.1. Unlimited polynomial reconstruction $\mathbb{P}_4$, $\mathcal{R}_{HO}$

For finite volume schemes, piece-wise polynomial were developed for years to achieve high accuracy in space. The piece-wise parabolic method (PPM) was developed in [13, 33, 43], for which second-order polynomials ($\mathbb{P}_2$) are implemented to obtain third-order accuracy. Furthermore, the piece-wise quartic method (PQM) was developed for instance in [64], it is a fifth-order

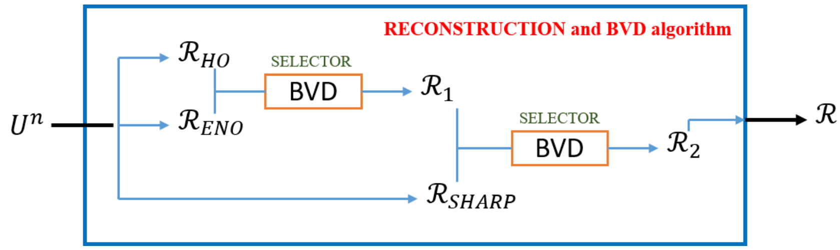

Figure 1: Sketch of Reconstruction schemes for Solution Property Preserving and BVD algorithm for a given cell. At stage 1, the BVD algorithm selects between $\mathcal{R}_{\mathrm{HO}}$ and $\mathcal{R}_{\mathrm{ENO}}$ reconstructions to get the most suitable of the two, say $\mathcal{R}_1$. Then, At stage 2, BVD chooses either reconstruction $\mathcal{R}_1$ or $\mathcal{R}_{\mathrm{SHARP}}$ to get $\mathcal{R}_2$ as the final reconstruction to be used to update the current cell.

accuracy scheme based on the piece-wise polynomial of degree four ($\mathbb{P}_4$) which we will use. Hence, the reconstructed values at the left and right cell boundaries, denoted as $U^{L,P4}_{i+1/2}$ and $U^{R,P4}_{i-1/2}$ respectively, are given by

$$\begin{aligned} U^{L,P4}_{i+1/2} &= \frac{1}{60}\left(2\,U_{i-2} - 13\,U_{i-1} + 47\,U_i + 27\,U_{i+1} - 3\,U_{i+2}\right), \\ U^{R,P4}_{i-1/2} &= \frac{1}{60}\left(-3\,U_{i-2} + 27\,U_{i-1} + 47\,U_i - 13\,U_{i+1} + 2\,U_{i+2}\right). \end{aligned} \tag{13}$$

This reconstruction can achieve 5th order accuracy on smooth enough profiles; unfortunately, it induces oscillatory when steep gradients are encountered. The stencil $\mathcal{S}_i$ is made of two neighbor cells to the left and right of I_i.

3.2. THINC reconstruction with $\beta \le 1.2$, ($\mathcal{R}_{ENO}$) or $\beta \ge 1.6$, ($\mathcal{R}_{SHARP}$)

One of the algebraic type VOF (volume of fluid) schemes built to capture moving interfaces in multi-phase flows, is known as THINC (Tangent of Hyperbola for INterface Capturing) method which employs hyperbolic tangent functions for spatial reconstruction [66, 67, 51]. The hyperbolic tangent function is a differentiable and monotone sigmoid function that mimics a step-like discontinuity. It has been shown in recent studies that with a properly chosen steepness factor, a THINC scheme performs well as an advection scheme with a competitive accuracy compared to classical TVD schemes [17]. The THINC reconstruction function can be expressed for a monotonically increasing or decreasing set of successive mean values (U_{i-1}, U_i, U_{i+1}) as [66, 53]

$$U_i(x) = \mathbb{U}_{\min} + \frac{\mathbb{U}_{\max}}{2}\left[1 + \Gamma \tanh\left(\beta\left(\frac{x - x_{i-1/2}}{x_{i+1/2} - x_{i-1/2}} - \widetilde{x}_i\right)\right)\right], \tag{14}$$

where $\mathbb{U}_{\min} = \min(U_{i-1}, U_{i+1})$, $\mathbb{U}_{\max} = \max(U_{i-1}, U_{i+1}) - \mathbb{U}_{\min}$, $\Gamma = \mathrm{sgn}(U_{i+1} - U_{i-1})$. The user-given parameter β is used for the control of the steepness and, consequently the jump thickness. In (14), the only remaining unknown is $\widetilde{x}_i$. It represents the location of the jump center and is determined by solving $U_i = \frac{1}{\Delta x}\int_{I_i} U_i(x)dx$, which is a volume-integrated average. After solving for $\widetilde{x}_i$, the reconstructed values at the left and right ends of cell I_i boundary can be defined by

$$\begin{aligned}
U^{L,Th\beta}_{i+1/2} &= U^{L,Th\beta}_{i}(x_{i+1/2}) = \mathbb{U}_{\min} + \frac{\mathbb{U}_{\max}}{2}\left(1 + \Gamma\frac{\tanh(\beta) + A}{1 + A\tanh(\beta)}\right), \\
U^{R,Th\beta}_{i-1/2} &= U^{R,Th\beta}_{i}(x_{i-1/2}) = \mathbb{U}_{\min} + \frac{\mathbb{U}_{\max}}{2}(1 + \Gamma A),
\end{aligned} \tag{15}$$

where $A = \frac{1}{\tanh(\beta)}\frac{B}{\cosh(\beta)-1}$, $B = e^{\Gamma\beta(2C-1)}$ and $C = \dfrac{U_i - \mathbb{U}_{\min} + \epsilon}{\mathbb{U}_{\max} + \epsilon}$ with $\epsilon = 10^{-20}$ to avoid division by zero. $U^{L,Th\beta}_{i+1/2}$ and $U^{R,Th\beta}_{i-1/2}$ are the reconstructed values for THINC candidate function using β parameter on the current cell boundaries.

Remark 1. The THINC reconstruction is in-bounds by construction since its stencil S_i considers only its direct neighbor cells I_{i-1} and I_{i+1}.

Remark 2. If U_i is a local extremum, we naturally set $U_i(x) = U_i$ for all $x \in I_i$. We could improve this further by the use of one TVD reconstruction for instance.

THINC reconstruction with $\beta \leq 1.2$: $\mathcal{R}_{ENO}$. In order to avoid oscillatory behavior we employ a THINC reconstruction with small values of parameter β. The operators are respectively denoted by $\mathcal{R}_{\mathrm{ENO}_2}$ with $\beta = 1.2$ and $\mathcal{R}_{\mathrm{ENO}_1}$ with $\beta = 1.1$. These values, $\beta = 1.2$ and $\beta = 1.1$, are small enough and correspond more or less, to the same dissipation than a second order TVD scheme with either the (slightly compressive) Van Leer slope limiter or the (dissipative) Minmod one, respectively, see [17, 16, 55].

THINC reconstruction with $\beta \geq 1.6$: $\mathcal{R}_{SHARP}$. The last THINC reconstruction operator in this paper employs $\beta = 1.6$ to capture sharper discontinuities or shocks by using the staircase/squaring behavior. The associated finite volume scheme using the reconstruction operator $\mathcal{R}_{\mathrm{SHARP}}$ is then genuinely anti-dissipative, leading to staircase shapes even for smooth profiles, so it must be employed only in the vicinity of discontinuity.

3.3. *Piecewise Constant/no reconstruction* $\mathbb{P}_0$, $\mathcal{R}_{LO}$

The piece-wise constant "reconstruction" leads to a first-order finite volume method that produces monotone and extremely robust numerical solutions, usually preserving the admissible physical set (i.e positivity of density and specific energy for Euler equations). We denote the $\mathbb{P}_0$ reconstruction as $U^{L,P0}_{i+1/2} = U^{R,P0}_{i-1/2} = U_i$. It is employed as the last resort solution when dealing with extreme phenomena or situations violating the physics, for instance, a lack of positivity, an occurrence of `NaN`, etc. see section 3.5.

In table 1, the five candidate reconstructions are listed with their different behaviors; on smooth solutions, to suppress spurious oscillations, on discontinuous solutions, and to handle demanding situations.

Acronym	**Reconstruction**	**Parameter**	**Solution property**
$\mathcal{R}_{\text{HO}}$	$\mathbb{P}_k \Rightarrow$ unlimited polynomial	$k = 4$	smooth profile
$\mathcal{R}_{\text{ENO}_2}$	THINC	$\beta = 1.2$	(damp) spurious oscillations
$\mathcal{R}_{\text{ENO}_1}$	THINC	$\beta = 1.1$	(kill) spurious oscillations
$\mathcal{R}_{\text{SHARP}}$	THINC	$\beta = 1.6$	steep profile
$\mathcal{R}_{\text{LO}}$	$\mathbb{P}_k \Rightarrow$ no reconstruction	$k = 0$	ensure admissible solution (i.e positivity issue, `NaN`)

Table 1: Table of reconstructions and their associated target property.

3.4. *A 3-stage BVD algorithm: local reconstruction selector*

As already mentioned the selector determining which reconstruction operator to use in each cell is based on the Boundary Variation Diminishing (BVD) algorithm [53, 17, 15, 16]. In this work, the selection algorithm in the P4-THINC-BVD-MOOD scheme designed in [55] is re-used. It determines the candidate interpolant with three-stages cascade BVD process which minimizes the total boundary variation (TBV) in the desired cell. More precisely the TBV of cell I_i is defined by the sum of the jumps generated by the reconstructed values using reconstruction operator $\mathcal{R}$ at cell interfaces, that is

$$\text{TBV}^{\mathcal{R}}_i(U) = \left|U^{L,\mathcal{R}}_{i-1/2} - U^{R,\mathcal{R}}_{i-1/2}\right| + \left|U^{L,\mathcal{R}}_{i+1/2} - U^{R,\mathcal{R}}_{i+1/2}\right| \geq 0. \tag{16}$$

Each term of the right hand side represents the amount of dissipation introduced by the numerical flux (9) for one edge of cell I_i. Thus $\mathrm{TBV}_i^{\mathcal{R}}$ scales like the numerical dissipation in the cell. For simplicity of exposition, we denote by $\mathcal{R}_{\mathrm{ST}_1}$, $\mathcal{R}_{\mathrm{ST}_2}$, and $\mathcal{R}_{\mathrm{ST}_3}$ the reconstruction operators in cell I_i after the first, second and third stage, respectively. For instance, when two reconstructions $\mathcal{R}_1$ and $\mathcal{R}_2$ of the same data U are available then we compute, compare $\mathrm{TBV}_i^{\mathcal{R}_1}$ and $\mathrm{TBV}_i^{\mathcal{R}_2}$, and choose the least dissipative one. The BVD algorithm automatically exploits this matter.

The 3-stage BVD algorithm is implemented in the spirit of [15, 16, 55]. Let us denote by r_i the actual reconstruction employed in cell I_i which can be HO, ENO_1, ENO_2, or SHARP.

Stage 1. Selection between $\mathcal{R}_{\mathrm{HO}}$ and $\mathcal{R}_{\mathrm{ENO}_2} \to \mathcal{R}_{\mathrm{ST}_1}$

Compute the TBV_i values for the cell I_i by $\mathcal{R}_{\mathrm{HO}}$ and $\mathcal{R}_{\mathrm{ENO}_2}$ as

$$\begin{aligned}
\mathrm{TBV}_i^{\mathcal{R}_{\mathrm{HO}}} &= \left|U_{i-1/2}^{L,\mathcal{R}_{\mathrm{HO}}} - U_{i-1/2}^{R,\mathcal{R}_{\mathrm{HO}}}\right| + \left|U_{i+1/2}^{L,\mathcal{R}_{\mathrm{HO}}} - U_{i+1/2}^{R,\mathcal{R}_{\mathrm{HO}}}\right| \\
\mathrm{TBV}_i^{\mathcal{R}_{\mathrm{ENO}_2}} &= \left|U_{i-1/2}^{L,\mathcal{R}_{\mathrm{ENO}_2}} - U_{i-1/2}^{R,\mathcal{R}_{\mathrm{ENO}_2}}\right| + \left|U_{i+1/2}^{L,\mathcal{R}_{\mathrm{ENO}_2}} - U_{i+1/2}^{R,\mathcal{R}_{\mathrm{ENO}_2}}\right|
\end{aligned} \tag{17}$$

For cell i, if $\mathrm{TBV}_i^{\mathcal{R}_{\mathrm{HO}}} > \mathrm{TBV}_i^{\mathcal{R}_{\mathrm{ENO}_2}}$ then $(\mathrm{r}_{i-1}, \mathrm{r}_i, \mathrm{r}_{i+1}) = \mathrm{ENO}_2$, else $\mathrm{r}_i = \mathrm{HO}$.

$\mathcal{R}_{\mathrm{ST}_1} = \{\mathrm{r}_i,\, i = 1, \ldots, N\}$

Stage 2. Selection between $\mathcal{R}_{\mathrm{ST}_1}$ and $\mathcal{R}_{\mathrm{ENO}_1} \to \mathcal{R}_{\mathrm{ST}_2}$

Compute the TBV_i values for the cell I_i by $\mathcal{R}_{\mathrm{ST}_1}$ and $\mathcal{R}_{\mathrm{ENO}_1}$ as

$$\begin{aligned}
\mathrm{TBV}_i^{\mathcal{R}_{\mathrm{ST}_1}} &= \left|U_{i-1/2}^{L,\mathcal{R}_{\mathrm{ST}_1}} - U_{i-1/2}^{R,\mathcal{R}_{\mathrm{ST}_1}}\right| + \left|U_{i+1/2}^{L,\mathcal{R}_{\mathrm{ST}_1}} - U_{i+1/2}^{R,\mathcal{R}_{\mathrm{ST}_1}}\right| \\
\mathrm{TBV}_i^{\mathcal{R}_{\mathrm{ENO}_1}} &= \left|U_{i-1/2}^{L,\mathcal{R}_{\mathrm{ENO}_1}} - U_{i-1/2}^{R,\mathcal{R}_{\mathrm{ENO}_1}}\right| + \left|U_{i+1/2}^{L,\mathcal{R}_{\mathrm{ENO}_1}} - U_{i+1/2}^{R,\mathcal{R}_{\mathrm{ENO}_1}}\right|
\end{aligned} \tag{18}$$

Similar to stage 1, for cell i, if $\mathrm{TBV}_i^{\mathcal{R}_{\mathrm{ST}_1}} > \mathrm{TBV}_i^{\mathcal{R}_{\mathrm{ENO}_1}}$ then $(\mathrm{r}_{i-1}, \mathrm{r}_i, \mathrm{r}_{i+1}) = \mathrm{ENO}_1$.

$\mathcal{R}_{\mathrm{ST}_2} = \{\mathrm{r}_i,\, i = 1, \ldots, N\}$

Stage 3. Selection between $\mathcal{R}_{\mathrm{ST}_2}$ and $\mathcal{R}_{\mathrm{SHARP}} \to \mathcal{R}_{\mathrm{ST}_3}$

Compute the TBV_i values for the cell I_i by $\mathcal{R}_{\mathrm{ST}_2}$ and $\mathcal{R}_{\mathrm{SHARP}}$ as

$$\begin{aligned}
\mathrm{TBV}_i^{\mathcal{R}_{\mathrm{ST}_2}} &= \left|U_{i-1/2}^{L,\mathcal{R}_{\mathrm{ST}_2}} - U_{i-1/2}^{R,\mathcal{R}_{\mathrm{ST}_2}}\right| + \left|U_{i+1/2}^{L,\mathcal{R}_{\mathrm{ST}_2}} - U_{i+1/2}^{R,\mathcal{R}_{\mathrm{ST}_2}}\right| \\
\mathrm{TBV}_i^{\mathcal{R}_{\mathrm{SHARP}}} &= \left|U_{i-1/2}^{L,\mathcal{R}_{\mathrm{SHARP}}} - U_{i-1/2}^{R,\mathcal{R}_{\mathrm{SHARP}}}\right| + \left|U_{i+1/2}^{L,\mathcal{R}_{\mathrm{SHARP}}} - U_{i+1/2}^{R,\mathcal{R}_{\mathrm{SHARP}}}\right|
\end{aligned} \tag{19}$$

For cell i, if $\mathrm{TBV}_i^{\mathcal{R}_{\mathrm{ST}_2}} > \mathrm{TBV}_i^{\mathcal{R}_{\mathrm{SHARP}}}$ then $\mathrm{r}_i = \mathrm{SHARP}$.

$\mathcal{R}_{\mathrm{ST}_3} = \{\mathrm{r}_i,\, i = 1, \ldots, N\}$

Remark 1. According to the formulation of this method, the essentially oscillation-free solution is obtained after stage 1 and 2. In addition, the numerical dissipation at discontinuous/steep gradients is reduced after stage 3, if needed. It means that the desired properties are reinforced respectively at different stages by the multi-stage BVD algorithm.

Remark 2. In this paper, we employ the BVD algorithm independently for each characteristic variables [15, 16], however, one could also consider the implementation of BVD algorithm with a dependency among the reconstructed variables such as in [55]. Our numerical experiments reveal that our approach can achieve optimal high order, however, it may produce slightly noisy and diffusive results in some cases.

Remark 3. In the multi-stage BVD the THINC reconstruction with small β values (ENO) as $\beta = 1.1$ or $\beta = 1.2$ could be replaced by another TVD scheme. Contrarily, the unlimited high order polynomial reconstruction (HO) and THINC with high β value (SHARP) as $\beta = 1.6$ are mandatory operators. The HO one ensures the highest possible accuracy for smooth profiles, while the SHARP one is efficient, robust scheme and steepens discontinuous profiles.

3.5. Positivity-preserving and physical admissibility via an a posteriori MOOD algorithm

The last property of paramount importance is the ability to handle or deal with extreme physical and numerical situations such as the lack of positivity for density or pressure for gas flows or the occurrence of un-representable digit values (`NaN`, `Inf`). The positivity-preserving or a fail-safe behavior is usually difficult to ensure *a priori* by the reconstruction operators which are employed in the multi-stage BVD algorithm. Here we use the so-called *a posteriori* Multi-dimensional Optimal Order Detection (MOOD) algorithm [10, 19, 21]. In a MOOD procedure, the non-oscillatory behavior and physics admissibility are ensured via a list of criteria detecting the problematic or troubled cells. Being an *a posteriori* limiting procedure, it is performed after the computation of a candidate solution at t^{n+1}. The detection procedure checks whether the candidate solution $U_i^{n+1,*}$ satisfies the criteria for each cell. The cells where they are satisfied, are marked as 'valid' cells, and, the numerical solution is accepted: $U_i^{n+1} = U_i^{n+1,*}$. Contrarily the cells which do not pass the criteria are marked as 'troubled'. A troubled cell is locally recomputed starting again at time t^n but using the first-order Godunov scheme (piecewise constant reconstruction), see in figure 2. This first-order finite volume scheme produces an excessive

numerical viscosity and tends to smear out the flow structures. However, it is conservative, monotone, robust and positivity-preserving.
In addition, the detection is split into a Physical Admissible Detection (PAD) and Numerical Admissible Detection (NAD). The PAD is based on the physical properties to ensure that a solution is admissible. For Euler system of equations the physical admissibility is related to the positivity of density ρ and pressure p. More precisely, a cell is PAD troubled if $\rho_i^{n+1,*} \leq 0$ or $p_i^{n+1,*} \leq 0$. In addition, for the reacting Euler equations, a cell may be PAD troubled if $\alpha_i^{n+1,*} < 0$, where α is the mass fraction, otherwise the cell is eligible. The NAD checks if a cell is such that $U_i^{n+1,*} = \texttt{NaN}$ then it is flagged as NAD troubled, otherwise the cell is valid.

Once a cell I_i is troubled, then, as already mentioned, it is locally recomputed by the first-order Godunov scheme. Its direct neighbors are also marked as troubled cells for safety reason.

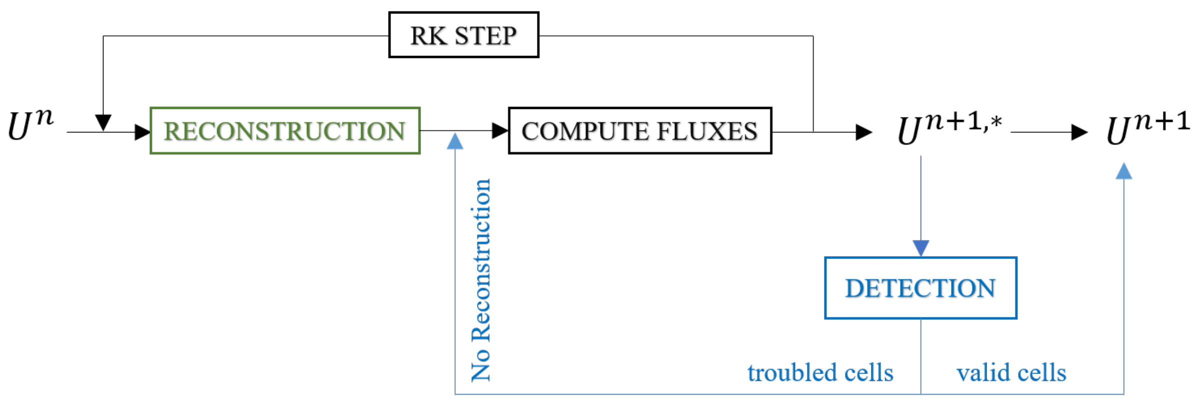

Figure 2: Sketch of FV method with an *a posteriori* MOOD algorithm. If the positivity is violated or a `NaN` is occurring, the Detection procedure (PAD or NAD) marks the troubled cells. Then, those troubled cells and their direct neighbors are sent back to t^n for a re-computation by the first order Godunov scheme (using $\mathbb{P}_0$ reconstruction). Otherwise, the valid cells are accepted as the final solution.

4. Extensions to multi-space dimensions

We have implemented and extended the previous numerical scheme in two-dimensions on structured grids. The scheme in 1D has been designed to be genuinely efficient, accurate and limiter-free, to sharply capture the shocks and steep gradients, and, to be robust when extreme events occur (near-vacuum states for instance). Our aim is to maintain these properties for the two-dimensional extension.

The two dimensional Euler equations with source terms are given by

$$\frac{\partial U}{\partial t} + \frac{\partial F(U)}{\partial x} + \frac{\partial G(U)}{\partial y} = S(U); \qquad t \geq 0, \qquad x, y \in \mathbb{R} \tag{20}$$

where $U = (\rho, \rho u, \rho v, E)^T$, $F(U) = [\rho u, \rho u^2 + p, \rho uv, (E+p)u]^T$, $G(U) = [\rho u, \rho uv, \rho v^2 + p, (E+p)v]^T$ and ρ, u,v, p are the density, velocity in x and y directions and pressure, respectively. E is the total energy and e is the internal energy. The pressure is linked to two thermodynamic variables via the perfect gas equation of state with adiabatic gas constant γ. Also, $S(U)$ are the source terms which are detailed in the next section: gravity, or two chemical state reaction.

Similar to 1D case, we employ the fractional step approach for gravity and second order Strang-splitting method [52] for chemical reaction source terms. For instance, the numerical solution at each time step level is computed in two steps: The homogeneous conservation law (convection step) and ODE system (source term or reaction step), successively. The two dimensional convection operator C approximates the solution of the homogeneous system on the time interval $[t^n, t^{n+1}]$. For the convection step, we consider the computational domain in space as a rectangular box $\Omega = [x^L, x^R] \times [y^L, y^R]$ divided into rectangular uniform cells $I_{i,j} = [x_{i-1/2}, x_{i+1/2}] \times [y_{j-1/2}, y_{j+1/2}]$. We denote the cell center by (x_i, y_j) and the cell sizes $\Delta x = x_{i+1/2} - x_{i-1/2}$ and $\Delta y = y_{j+1/2} - y_{j-1/2}$. For standard finite volume semi-discretization, we employ the volume integrated-average (VIA) of the numerical solution $U(x, y, t)$ over a mesh cell $I_{i,j}$ at time t by a piece-wise constant value

$$U_{i,j}(t) = \frac{1}{\Delta x \, \Delta y} \int\limits_{I_{i,j}} U(x, y, t) \, dx \, dy \qquad \text{where} \qquad i = 1, 2, \ldots, M, \qquad j = 1, 2, \ldots, N. \tag{21}$$

Similar to 1D, the VIA $U_{i,j}(t)$ for each mesh cell $I_{i,j}$ is updated by

$$\frac{dU_{i,j}(t)}{dt} = -\frac{1}{\Delta x} \left(F_{i+1/2,j}(t) - F_{i-1/2,j}(t)\right) - \frac{1}{\Delta y} \left(G_{i,j+1/2}(t) - G_{i,j-1/2}(t)\right), \tag{22}$$

where $F_{i\pm1/2,j}(t)$ and $G_{i,j\pm1/2}(t)$ are the two-point fluxes in x and y direction, respectively. They are computed like their 1D counterparts, that is a Riemann solver is further used to get

$$F_{i+1/2,j}(t) = F^{\text{Riemann}}_{i+1/2,j} \left(U^L_{i+1/2,j}, U^R_{i+1/2,j}, t\right). \tag{23}$$

where $U^L_{i+1/2,j}$ and $U^R_{i+1/2,j}$ are the left-side and right-side values of $U_{i,j}(x, y, t)$ at cell boundary in x direction respectively. The same procedure is employed in y-direction to compute the fluxes $G_{i,j+1/2}(t)$. In this work, the HLLCM Riemann solver [48] is employed. Similar to 1D section, the third-order TVD Runge-Kutta method (RK3, see [49, 30]) is used for high accurate time integration.

In 2D the reconstructions are performed direction by direction. In other words, the same $\mathbb{P}_4$ reconstructions as described in (13) are first made for data aligned in x direction: $U_{i-2,j}$, $U_{i-1,j}$, $U_{i,j}$, $U_{i+1,j}$, $U_{i+2,j}$, to get the edge centered values $U^L_{i+1/2,j}$ and $U^R_{i-1/2,j}$ for cell $I_{i,j}$. Then, the 1D reconstructions in y direction consider y-aligned data $U_{i,j-2}$, $U_{i,j-1}$, $U_{i,j}$, $U_{i,j+1}$, $U_{i,j+2}$ to get values $U^L_{i,j+1/2}$ and $U^R_{i,j-1/2}$ in cell $I_{i,j}$.

The THINC reconstructions are exactly the same as in 1D, their stencils are thus restricted to two aligned neighbor cells only. The *a posteriori* MOOD loop operates also alike. The local selection of reconstruction operator follows the same algorithm as in 1D and the selection of reconstruction operator is independent in x and y directions.

In the present work, the 2D scheme is constructed via a simple but efficient direction-by-direction extension. Indeed the flux integration along the edges is calculated using only one integration point at the edge center. So, the 2D scheme is formally of maximal second order accuracy.

Recall that the goal in this work is not to build a genuine 5th order accurate numerical method. On the contrary, we aim at building a genuine simple, efficient, robust and accurate enough scheme emphasizing that an appropriate mixing of linear and non-linear reconstruction operators may replace classical limiting techniques (such as slope/flux limiters, artificial viscosity, WENO, etc.). In previous works [16, 35], it has been observed that the present BVD scheme can maintain a high order of accuracy on smooth profiles of the advection equation in 1D and 2D. Moreover the comparison of dispersion and dissipation relations with respect to other schemes (TVD, WENO, WENO-Z) have been conducted and it was shown that the current scheme has comparable behaviors. Extensive numerical tests have been conducted in previous works such as [16, 35, 17, 55] to assess the appropriate behavior of this BVD scheme on classical 1D and 2D test cases. One can find the tables of convergence rate for the present scheme as well as the simulation of the standard 2D isentropic vortex problem and simpler advection tests in 2D in references

[16, 35]. Moreover some classical numerical results for the homogeneous Euler equations are reported in [55]: Sod, Lax, Le Blanc shock tubes, 2D Sedov blastwave, Double Mach reflection problem, shock-vortex interaction, shock/diffraction problem. The following numerical section provides some numerical evidences mainly in the non homogeneous case.

5. Numerical Experiments

In this section, we test the performance of the numerical scheme on some benchmark test problems of Euler system of PDEs with perfect gas EOS ($\gamma = 7/5$ or $5/3$) without or with various source terms. The finite volume numerical scheme is built under the following key tools: the reconstruction process is conducted in terms of characteristic decomposition, the HLLCM Riemann solver [48] is employed for the flux computation, a TVD-RK3 of third order for time integration, the BVD algorithm is used for the selector of space reconstructions, and, at last, an *a posteriori* MOOD loop is implemented for physical admissibility. For homogeneous Euler equations it consists of a the PAD criterion, that is the positivity preservation, while for the reactive Euler equations we must add the positivity of the mass fraction $\alpha_i^n \geq 0$.

5.1. Homogeneous Euler Equations

5.1.1. 2D explosion test

An axi-symmetric two dimensional explosion problem described in [58, 72] is first simulated. The computational domain is $\Omega = [-1, 1] \times [-1, 1]$ and the initial condition is given by

$$(\rho_0, u_0, v_0, p_0) = \begin{cases} (1,\ 0,\ 0,\ 1) & \text{if } r \leq R, \\ (0.125,\ 0,\ 0,\ 0.1) & \text{otherwise}, \end{cases} \tag{24}$$

where $r = \sqrt{x^2 + y^2}$ is the distance to the center of computational domain and $R = 0.5$. The fluid with high density and pressure inside the circle $R = 0.5$ spreads out into three circular waves: a diverging shock, followed by a diverging contact discontinuity and a converging rarefaction wave. The simulation runs up to $t_{\text{final}} = 0.2$ with a uniform grid made of 400×400 cells. In figure 3, we show the bird's eye view of density distribution and the cross-section profile

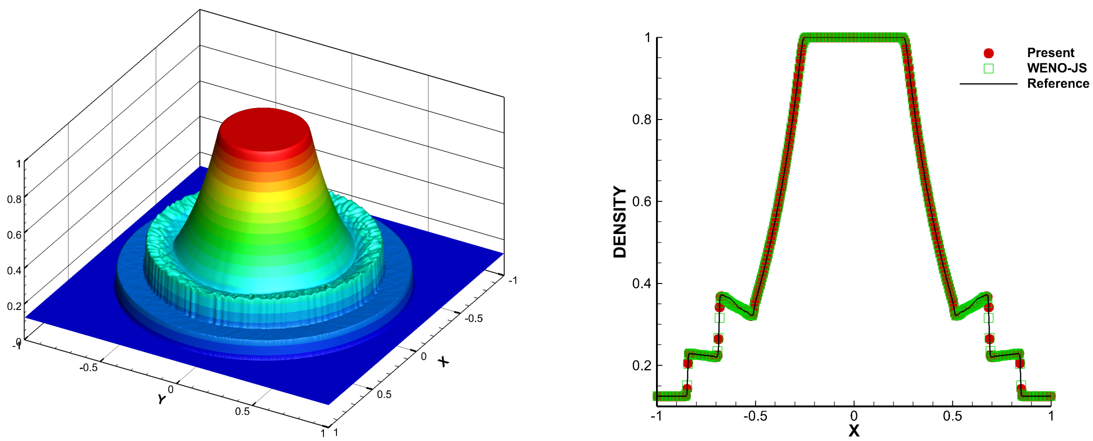

Figure 3: Numerical results for 2D explosion test – Density variable — Left: bird's eye view of density distribution computed by present scheme; Right: Cut-off profile along the radial direction.

along the radial direction. From the results, we observe that the present scheme captures the contact discontinuity and the shock wave without spurious oscillations and maintain the cylindrical symmetry. Moreover, compared to the reference WENO-JS scheme [34] (right panel), the present scheme captures a slightly sharper contact discontinuity.

5.1.2. 2D Riemann problems

In order to test the multi-stage BVD-MOOD scheme (accuracy, oscillatory-free and robustness), we simulate a set of two-dimensional Riemann problems (RP) which have been introduced and extensively studied in [38, 39, 47]. The computational domain is $\Omega = [-0.5, 0.5] \times [-0.5, 0.5]$ and the initial conditions made of 2×2 constant states are given by

$$U(x, y, t = 0) = \begin{cases} U_1 & \text{if} \quad x > 0 \wedge y > 0, \\ U_2 & \text{if} \quad x \leq 0 \wedge y > 0, \\ U_3 & \text{if} \quad x \leq 0 \wedge y \leq 0, \\ U_4 & \text{if} \quad x > 0 \wedge y \leq 0. \end{cases} \tag{25}$$

The initial conditions and the final solution time t_{final} for the four configurations are listed in Table 2. The ratio of specific heats is set to $\gamma = 1.4$. The simulations are run with a uniform grid made of 600×600 mesh cells with the CFL number 0.4 in all calculations. We compare our

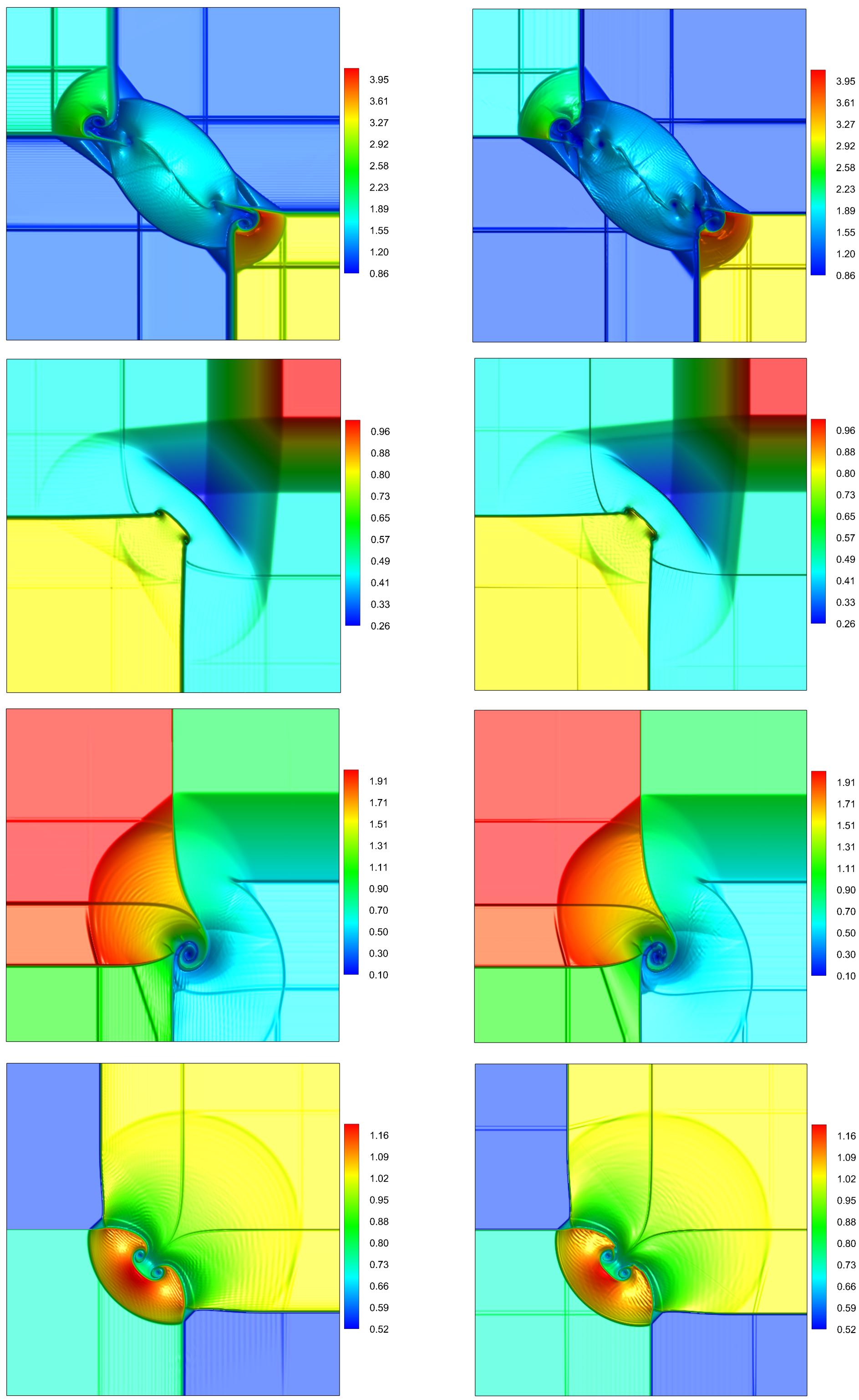

Figure 4: Numerical results for Riemann problems 1,2,3,4 – Density variable — Left: WENO-JS scheme; Right: Present scheme.

#		ρ	u	v	p	ρ	u	v	p	t_{final}
		$x \leq 0$				$x > 0$				
RP1	$y > 0$	2.0	-0.75	0.5	1.0	1.0	-0.75	-0.5	1.0	0.23
	$y \leq 0$	1.0	0.75	0 .5	1.0	3.0	0.75	-0.5	0.3	
RP2	$y > 0$	0.5197	-0.6259	0.1	0.4	1.0	0.1	0.1	1.0	0.25
	$y \leq 0$	0.8	0.1	0.1	0.4	0.5197	0.1	-0.6259	0.4	
RP3	$y > 0$	0.5313	0.8276	0.0	0.4	1.0	0.1	0.0	1.0	0.30
	$y \leq 0$	0.8	0.1	0.0	0.4	0.5313	0.1	0.7276	0.4	
RP4	$y > 0$	2.0	0.0	-0.3	1.0	1.0	0.0	-0.4	1.0	0.30
	$y \leq 0$	1.0625	0.0	0.2145	0.4	0.5197	0.0	-1.1259	0.4	

Table 2: Initial conditions for the 2D Riemann problems (RP) numbered from 1 to 4. These data correspond to Configurations 5, 7, 11 and 17 in [38].

numerical solution against the reference scheme WENO-JS from [34]. The numerical results for the density variable are shown in figure 4. In the left and right panels, we display the numerical density at the final time with the same scale and color for the WENO-JS and BVD-MOOD schemes respectively. A reference solution can be found for instance in [37]. In figure 4, we can observe on the computational results of two schemes that they comparably capture the main flow structures of all 2D RPs. Therefore, the multi-stage BVD-MOOD scheme seems to perform well in shock capturing situation without spurious oscillations, and, in the smooth parts of flow without excessive numerical dissipation. Furthermore, the present scheme does capture sharper discontinuities, more pronounced small-scale structures, and, present the birth of the Kelvin-Helmholtz instability on the shear waves compared to WENO-JS scheme. This is an evidence of a lower dissipation.

5.1.3. Forward facing step (Mach 3 step tunnel)

We simulate the so-called forward facing step (FFS) benchmark test which was proposed by Woodward and Collela in [65]. In this test a right-moving Mach 3 shock in a tunnel impacts a forward step. The initial condition contains a uniform gas with density $\rho = 1.4$, pressure $p = 1$, velocity components $u = 3$, $v = 0$ and specific heat ratio $\gamma = 1.4$. The computational domain is a wind tunnel $\Omega = [0, 3] \times [0, 1]$ with a step of 0.2 units high located at 0.6 units away from the entrance of the tunnel. The inflow and outflow boundary conditions are applied at the entrance and the exit while reflective wall boundary conditions are imposed at the remaining boundaries. The solution of this test involves complex flow structures, density disturbances and shear flows due to the interactions among shocks with the boundaries. The simulation is run up to $t_{\text{final}} = 4$ as a final time with CFL number is 0.4. For this test, the mesh is made of uniform cells with mesh size $\Delta x = 1/160$ and $1/240$. In figure 5, we display the density variable at the final time calculated by the proposed scheme. On the top panel, we plot the 3D bird's eye view of density field on 1/240 mesh size, which shows the adequately resolved shock waves, and the vortices of the Kelvin-Helmholtz instabilities developing along the top shear wave. On the same figure, the middle panels show the numerical results of 1/160 and 1/240 mesh size respectively. The small scale flow structures are better captured with the finer grid results as expected, moreover the discontinuities (shocks, contact) seem to be sharply captured by our approach. Notice that there is no issue with positivity in this test.

5.2. Euler equations with gravity source terms

Let us consider Euler equations supplemented with standard gravity source terms in vertical y-direction for the thermally ideal gas, which is expressed as system (20) with $S(U) = (0, 0, \rho g, \rho v g)$ where g is gravity source set to $g = 1$ for 2D Rayleigh-Taylor instability and $g = -1$ for 2D double rarefaction waves with gravity.

5.2.1. Two-dimensional Rayleigh-Taylor Instability

The Rayleigh-Taylor instability contains both discontinuities and complex flow structures, see [28, 70, 68, 26]. In this test, the instability occurs on an interface between two fluids of different densities when an acceleration is directed from the heavier towards the lighter fluid. The computational domain is $\Omega = [0, 0.25] \times [0, 1]$ and the initial condition is given by

$$(\rho_0, u_0, v_0, p_0) = \begin{cases} (2,\ 0,\ -0.025\, a\, \cos(8\pi x),\ 1 + 2y) & \text{if } 0 \leq y \leq 1/2, \\ (1,\ 0,\ -0.025\, a\, \cos(8\pi x),\ y + 3/2) & \text{if } 1/2 \leq y < 1, \end{cases} \tag{26}$$

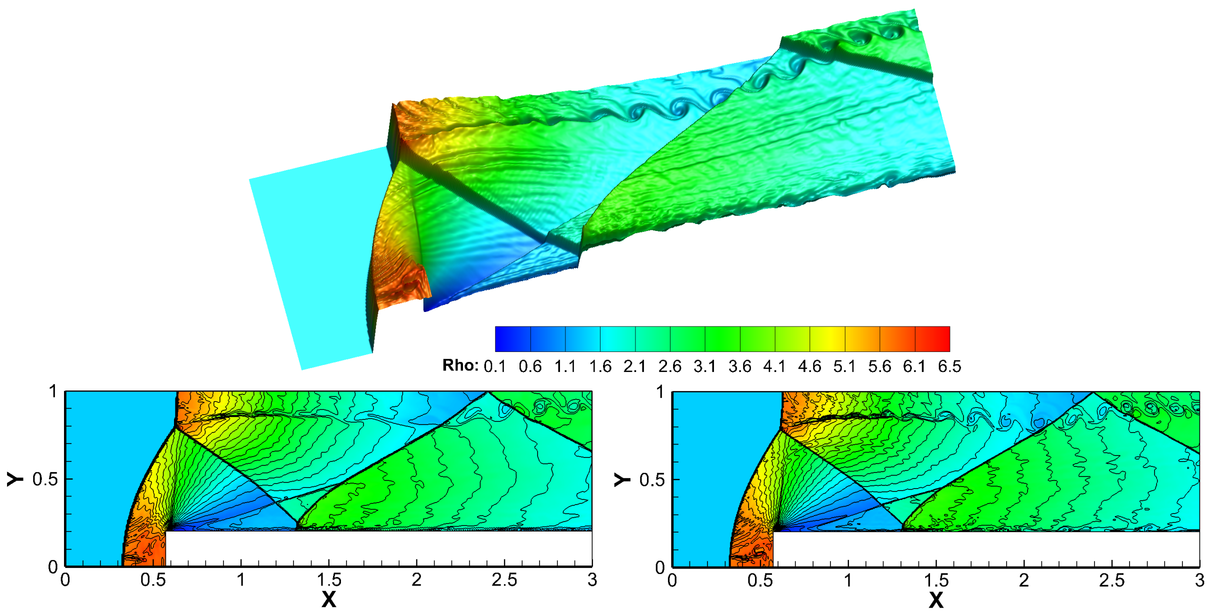

Figure 5: Numerical results for forward facing step problem at $t_{\text{final}} = 4$ simulated by the present scheme – Top-panel: Bird's eye view of density (color and elevation) with mesh size 1/240; Left-panel: 2D view, mesh size 1/160; Right-panel: 2D view, mesh size 1/240.

where $a = \sqrt{\gamma p/\rho}$ is the sound speed and the ratio of specific heat is set to $\gamma = 5/3$. Reflective boundary conditions are imposed for the left and right ends of the domain. On the upper boundary, we assign the primitive variables $(\rho, u, v, p) = (1, 0, 0, 2.5)$ and for the bottom boundary, we assign $(\rho, u, v, p) = (2, 0, 0, 1)$. The computational domain is discretized into a uniform 200×800 mesh. The fluid flow is simulated up to the final time $t_{\text{final}} = 1.95$ with CFL number 0.4. In figure 6, we display 15 uniform density contour lines spanning $[0.8, 2.3]$ for the WENO-JS (left panel) and the present scheme (right panel). We observe that the present scheme has resolved much richer vorticity structures than WENO-JS scheme. While the present scheme has a clear ability to resolve complex and small flow structures, however it induces some symmetry breaking probably due to the order dependency of the BVD algorithm, see [26].

5.2.2. Two-dimensional double rarefaction waves with gravity

The double rarefaction waves problem is a 2D Riemann problem which presents near vacuum state at the central zone as it involves two rarefaction fans moving in opposite directions [44, 73].

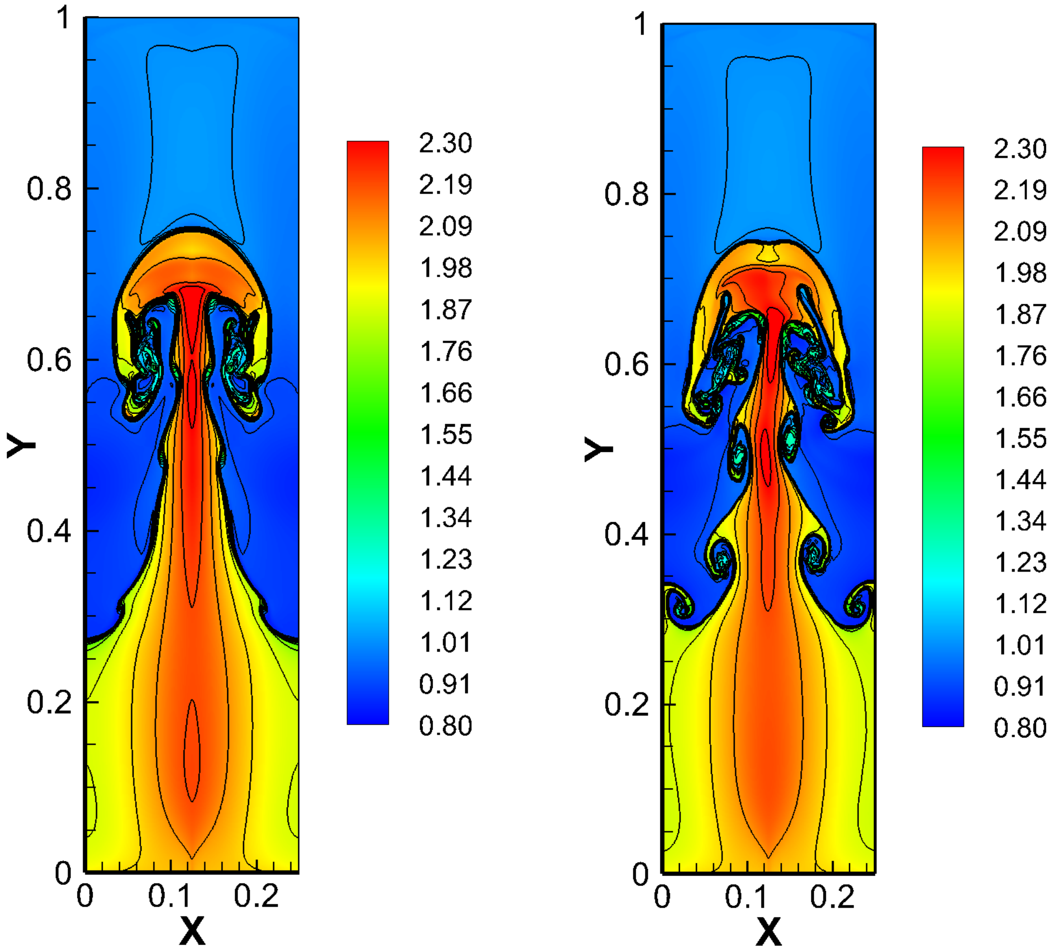

Figure 6: Density profile with 15 iso-contour lines for the Rayleigh-Taylor instability problem at $t_{\text{final}} = 1.95$. Left panel: WENO-JS scheme; Right panel: Present scheme.

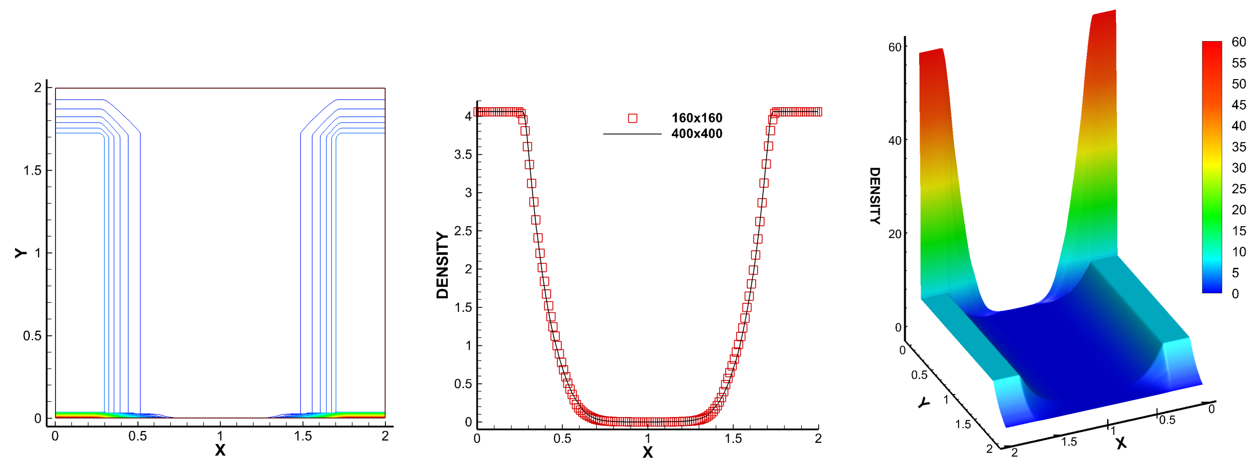

(a) (b) (c)

Figure 7: Numerical results for two-dimensional double rarefaction waves under gravity – (a) 60 equally spaced contour lines of density from 0 to 60; (b) the cutting lines along y-direction which is $y = 1.7875$, the solid line is the numerical solution fo 400×400 mesh and the symbol is the numerical solution of 80×80 mesh; (c) Bird's eye view for 3D density.

The initial condition on computational domain $\Omega = [0, 2] \times [0, 2]$ is given by [75]

$$(\rho_0, u_0, v_0, p_0) = \begin{cases} (7,\ -1,\ 0,\ 2) & \text{if } x \leq 1, \\ (7,\ 1,\ 0,\ 2) & \text{otherwise} \end{cases} \tag{27}$$

and the final time is set to $t_{\text{final}} = 0.6$ with CFL number set to 0.4 and $\gamma = 7/5$. The reflective boundary conditions are set on the top and bottom ends and outflow boundary conditions are set to the left and right ends of the computational domain. A mesh made of 80×80 cells is considered and a reference solution is obtained with 400×400 mesh cells. The numerical results are shown in figure 7. Due to the gravity source term pointing in the negative y direction, the numerical solution presents some expansion on the top part ($y \geq 1.6$) and compression on the bottom one ($y \leq 0.05$). The numerical solution is genuinely smooth and has a good agreement with the reference one. Moreover the obtained solution is comparable to the one in [75] without presenting any spurious effects in the central near vacuum state for which the density drops down to $\rho \simeq 5.72E - 06$.

5.3. The reactive Euler equations – Detonation waves

In this section, we show the numerical benchmark tests suite used in 1D and 2D for the reactive Euler equations. We set the CFL to 0.05 for WENO-JS scheme and to 0.1 for the present BVD+MOOD for the following test cases.

5.3.1. 1D reactive Euler equations

We consider the time-dependent inviscid compressible flow with reaction between two chemical states in one-dimensional space. The homogeneous Euler system (1) (i.e. with $S(U) = 0$) is supplemented with an equation on the mass fraction of the unburnt gas α as

$$\frac{\partial}{\partial t}(\rho\alpha) + \frac{\partial}{\partial x}((\rho\alpha)u) = K(T)\,(\rho\,\alpha) \tag{28}$$

where $K(T)$ is the chemical reaction rate. The pressure is obtained from an equation of state like

$$p = (\gamma - 1)\left(E - \frac{1}{2}\rho u^2 + \mathsf{R}\right), \tag{29}$$

where $\mathsf{R} = -q_0\,(\rho\alpha)$ models the heat released from the chemical reaction processes, and q_0 denotes the chemical heat release. The temperature is computed by $T = \frac{p}{\rho}$ and we set the γ to 1.4. The reaction rate $K(T)$ can be modeled with the so-called Arrhenius kinetics [60] as

$$K(T) = K_0 \exp\left(\frac{-T_{ign}}{T}\right), \tag{30}$$

where K_0 the pre-exponential coefficient and T_{ign} the ignition (or activation) temperature are model parameters. When the source term becomes stiff, the reaction rate may be modeled by a Heaviside kinetics as

$$K(T) = \begin{cases} \frac{1}{\xi} & \text{if} \quad T \geq T_{ign}, \\ 0 & \text{if} \quad T < T_{ign}, \end{cases} \tag{31}$$

where ξ represents the reaction time.

Chapman-Jouguet (C-J) detonation wave with Arrhenius Law. In this test, the Arrhenius source term (30) is employed, see [32, 60, 63, 18]. The initial condition consists of a completely burnt gas ($\alpha = 0$) on the left-hand side facing an un-burnt counterpart ($\alpha = 1$) on the right. The density, velocity and pressure of the un-burnt state are given by ($\rho_u = 1, u_u = 0, p_u = 1, \alpha_u = 1$). The heat release is set to $q_0 = 25$, the ignition temperature to $T_{ign} = 25$ and $K_0 = 16.418 \times 10^3$. We obtain the C-J initial state for the burnt state ($\rho_{CJ}, u_{CJ}, p_{CJ}, \alpha_{CJ} = 0$) following [9, 63]. The 1D computational domain is $\Omega = [0, 30]$ and the initial discontinuity is located at $x_d = 10$. The final time is $t_{\text{final}} = 1.8$ for which the detonation wave has reached location $x_d = 22.8$. The simulation was performed by the standard 5^{th} order WENO-JS scheme and the present multi-stage BVD-MOOD scheme both using $N = 300$ cells. The reference solution is calculated by WENO-JS scheme with 10000 cells and displayed in solid line in figure 8. In this figure we show the numerical results for the density, mass fraction, pressure and temperature for both schemes. We observe that the present scheme is able to capture the correct propagation speed of the C-J detonation wave with a larger CFL number whereas WENO-JS scheme produces spurious oscillations and errors linked to an extra dissipation (extra plateaus or wrong shock speed) in the vicinity of the discontinuity. Moreover, the WENO-JS numerical scheme inaccurately locates the discontinuity, and, as a consequence, produces a wrong physical solution. Contrarily the BVD-MOOD scheme, being less diffusive is able to capture the correct chronometry of the wave along with the expected numerical solution.

Chapman-Jouguet detonation wave with the Heaviside Model. In this example we consider the C-J detonation model for which the chemical reaction is in its Heaviside form. The parameter values of the model are taken from [12, 3, 63, 17] as $\frac{1}{\xi} = 0.5825 \times 10^{10}$, $q_0 = 0.5196 \times 10^{10}$, $T_{ign} = 0.1155 \times 10^{10}$ and $\gamma = 1.4$. The 1D computational domain is $\Omega = [0, 0.05]$ and the initial discontinuity is set at $x_d = 0.005$. The density, velocity and pressure of the un-burnt state are given by ($\rho_u = 1.201 \times 10^{-3}, u_u = 0, p_u = 8.321 \times 10^5, \alpha_u = 1$). The totally burned gas is located on the left side of the tube, where ($\rho_{CJ}, u_{CJ}, p_{CJ}, \alpha_{CJ} = 0$) are determined by the C-J detonation model. The computation is run up to final time $t_{\text{final}} = 3 \times 10^{-7}$ with a uniform mesh made of $N = 300$ cells. The exact position of the detonation wave is at $x_d = 0.03764$ at final time. We plot the results of the density, mass fraction, pressure and temperature variables for both schemes in figure 9 where the reference solution is computed by WENO-JS scheme with 10000 mesh cells. We observe that the detonation wave is correctly and sharply captured by the proposed scheme, whereas WENO-JS scheme produces a wrong numerical solution (even if

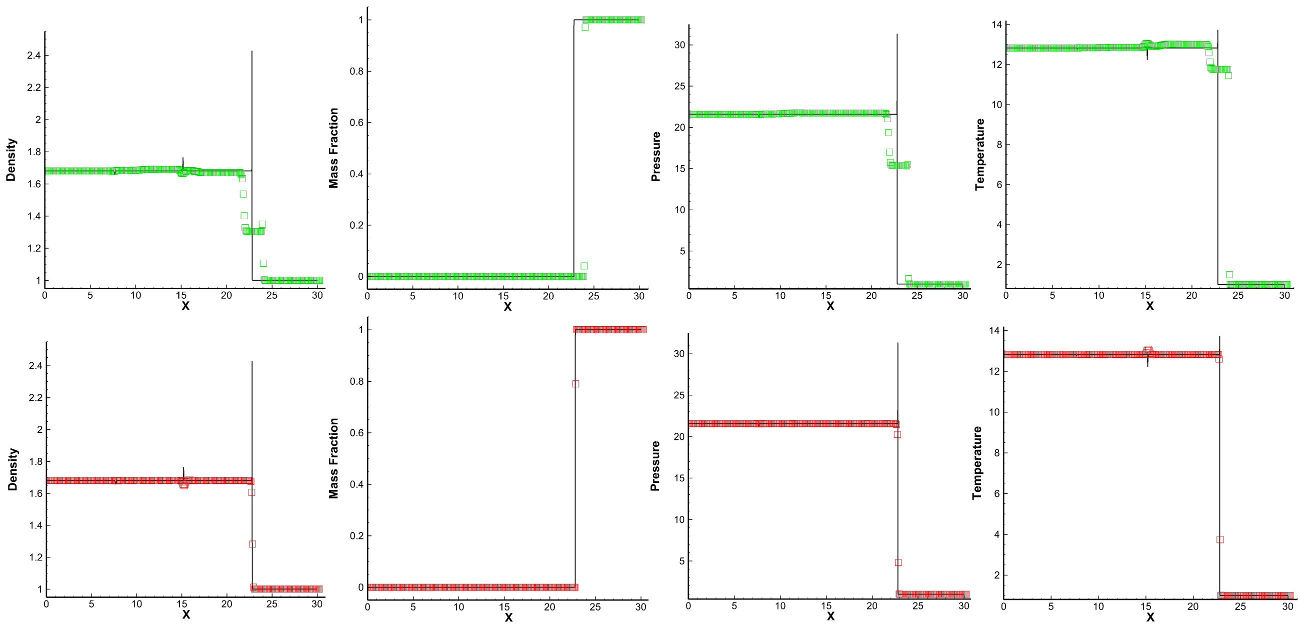

Figure 8: Numerical results for density, mass fraction, pressure and temperature of Arrhenius case at time $t_{\text{final}} = 1.8$ – Top: WENO-JS scheme (green symbols); Bottom: Present BVD-MOOD scheme (red symbols).

smaller time steps are used because the stiffness of detonation wave is emphasized by the spatial errors rather than the temporal ones), as already reported in [63].

Interaction between a detonation wave and an oscillatory profile (Heaviside model). In this section we consider the interaction between a detonation wave and an oscillatory profile which is taken from [2, 63, 17]. The parameter of this test are $\gamma = 1.2$, $q_0 = 50$, $\frac{1}{\xi} = 1000$, and $T_{ign} = 3$. The computational domain is $\Omega = [0, 2\pi]$ with a uniform mesh made of $N = 200$ cells. The initial condition is given by

$$(\rho_0, u_0, p_0, \alpha_0) = \begin{cases} (1.79463,\ 3.0151,\ 21.53134,\ 0) & \text{if } x \leq \frac{\pi}{2}, \\ (1 + 0.5\sin(2x),\ 0,\ 1,\ 1) & \text{otherwise.} \end{cases} \tag{32}$$

The numerical solution is calculated up to time $t_{\text{final}} = \frac{\pi}{5}$ and the reference solution is computed by WENO-JS scheme with 10000 mesh cells. In figure 10 we observe the occurrence of spurious waves produced by WENO-JS scheme. On the contrary the present BVD-MOOD scheme prevents their appearance. Furthermore, the present scheme is able to resolve the flow field

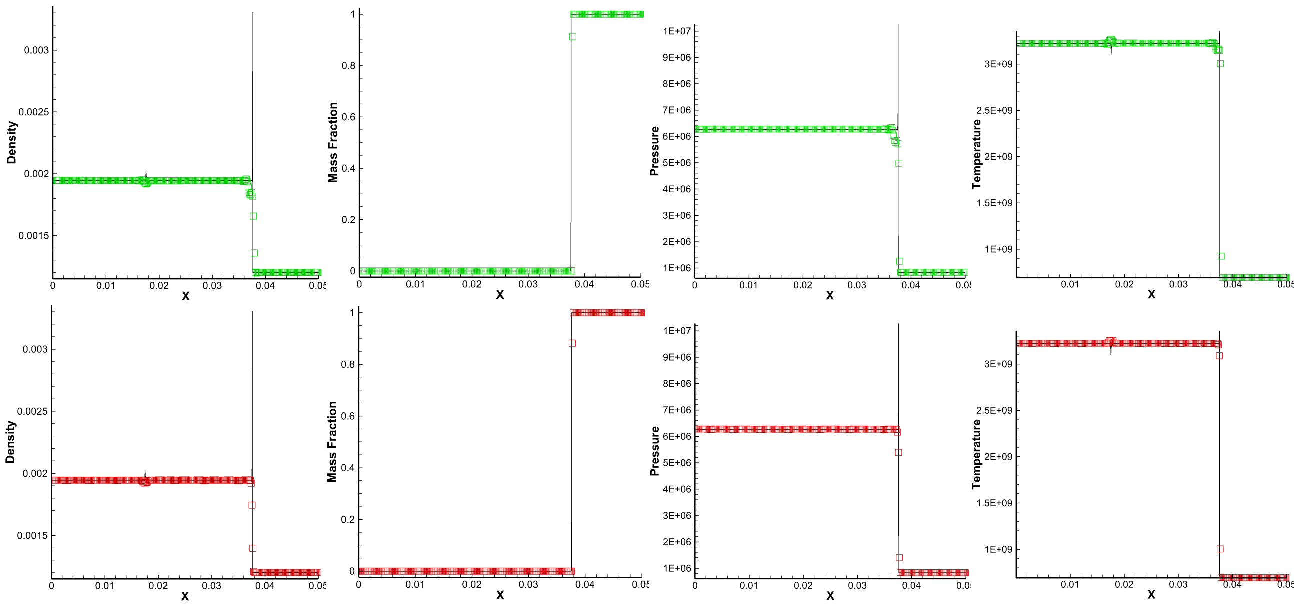

Figure 9: Same as figure 8, but for the Heaviside model at time $t_{\text{final}} = 3 \times 10^{-7}$.

produced after the interaction between the detonation wave and the oscillatory profile. At last the shock is again sharply captured.

Collision of two detonation waves. The last 1D reactive Euler model test case consists in a collision of detonation waves. It resembles the Woodward-Collela blastwave benchmark test used for the homogeneous Euler equations [13]. This test presents three constant states. The middle state is the un-burnt gas while the left and right high-density, high-pressure burnt gases moves towards the fresh middle state. At $t > 0$ it generates left and right moving detonation waves along with rarefaction fans and contacts after impinging on the burning fronts. After some time we observe the collision between two detonation waves. The parameter of the model are taken following [2], i.e $\gamma = 1.2$, $q_0 = 50$, $\frac{1}{\xi} = 230.75$, and $T_{ign} = 3$. The computational domain is $\Omega = [0, 100]$ meshed with uniform cells ($N = 200$). The initial condition is given by

$$(\rho_0, u_0, p_0, \alpha_0) = \begin{cases} (1.79463,\ 3.0151,\ 30,\ 0) & \text{if } x \leq 10, \\ (1,\ 0,\ 1,\ 1) & \text{if } 10 < x < 90, \\ (1.79463,\ -8,\ 21.53134,\ 0) & \text{if } 90 \leq x. \end{cases} \tag{33}$$

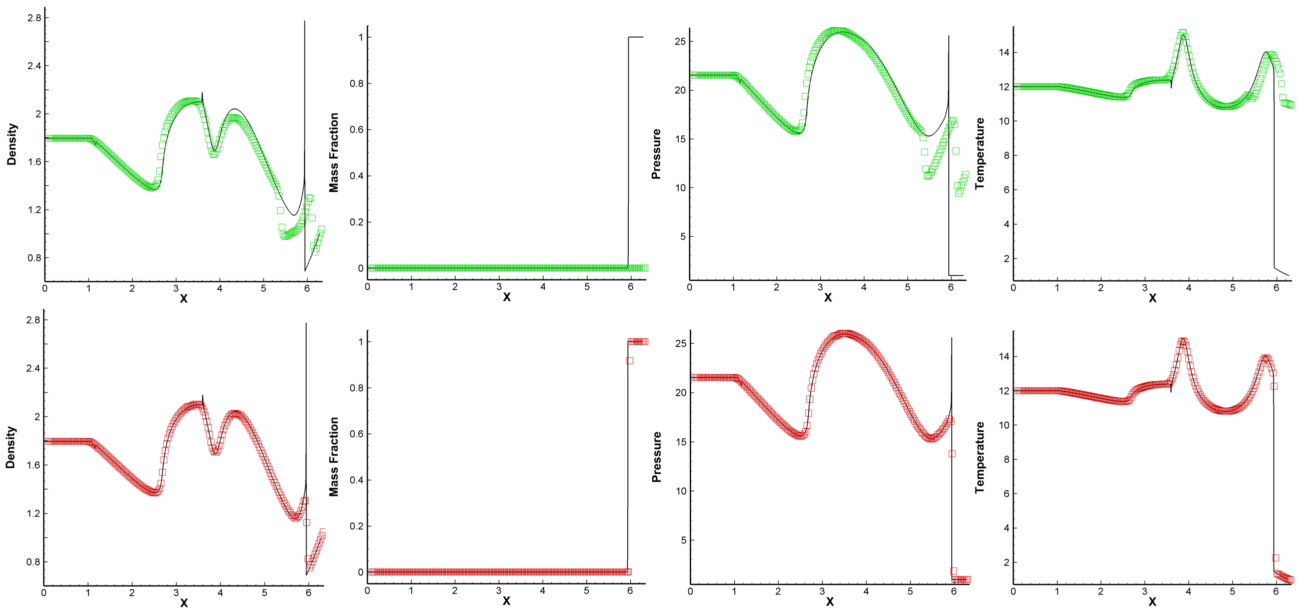

Figure 10: Numerical results for density, mass fraction, pressure and temperature of interaction between a detonation wave and an oscillatory profile at time $t_{\text{final}} = \frac{\pi}{5}$ – Top: WENO-JS scheme (green symbols); Bottom: Present BVD-MOOD scheme (red symbols).

The numerical solution is calculated up to time $t_1 = 4$ (before collision) in figure 11, and, time $t_2 = 6$ (after collision) in figure 12, respectively. The reference solution is computed by WENO-JS scheme with $N = 10000$ mesh cells. Density, mass fraction, pressure and temperature are displayed in the figures. Before and after the collisions, the BVD-MOOD scheme correctly and sharply captures the shocks, contacts and rarefaction waves in excellent agreement with the reference solution. On the contrary the WENO-JS scheme produces spurious supernumerary numerical waves which are unrelated to the model of PDEs. The embedded numerical diffusion of WENO-JS scheme incorrectly triggers the reaction which then produces a wrong numerical solution as can be seen: indeed, it can not capture the correct location of shock speed for instance. Notice that the left-most contact discontinuity is captured on less than two cells with BVD-MOOD scheme while WENO-JS demands about five cells. This extra numerical dissipation is responsible for the observed inappropriate behaviors. From these 1D numerical tests for reactive Euler equations, we can see that the BVD-MOOD scheme can accurately reproduce the complex wave structure of this model, moreover it captures sharply the contact

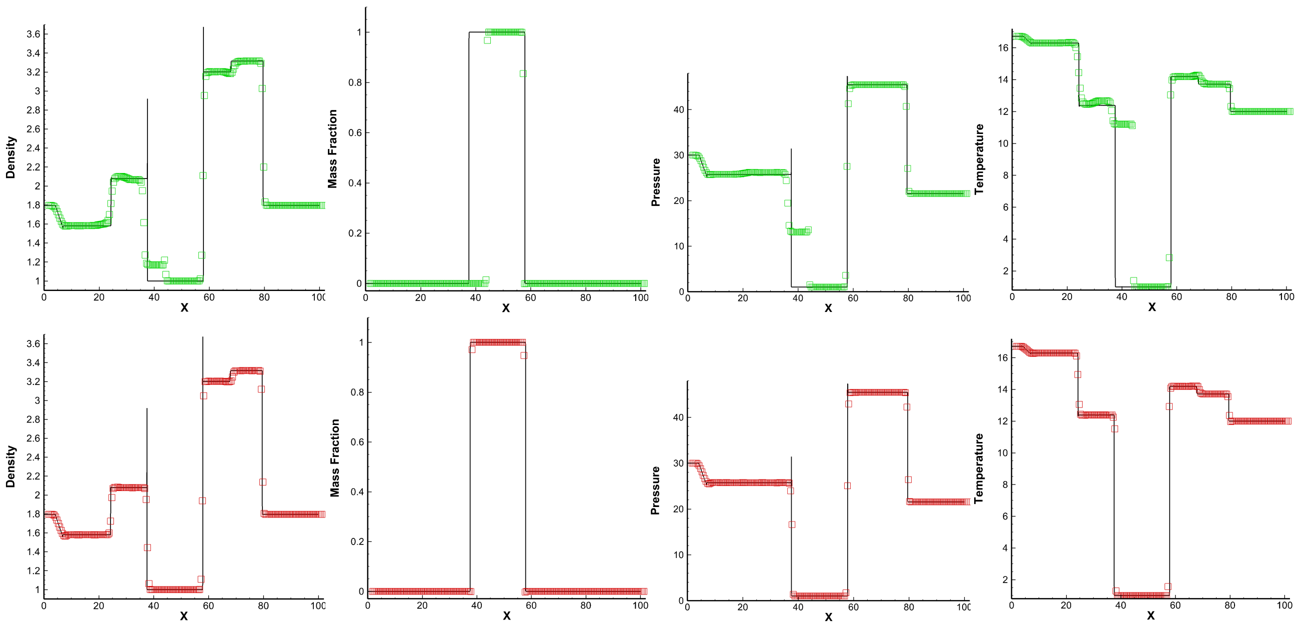

Figure 11: Numerical results for density, mass fraction, pressure and temperature of collision of two detonations — Before collision at time $t_1 = 4$ – Top: WENO-JS scheme (green symbols); Bottom: Present BVD-MOOD scheme (red symbols).

and material interfaces (on one or two cells), and can handle the interactions between simple waves: detonation waves, oscillatory smooth profiles, rarefactions and contacts.

5.3.2. 2D reactive Euler equations

The two-dimensional version of the previous 1D system considers (20) with $S(U) = 0$ supplemented with the 2D version of (28), i.e

$$\frac{\partial}{\partial t}(\rho\alpha) + \frac{\partial}{\partial x}((\rho\alpha)u) + \frac{\partial}{\partial y}((\rho\alpha)v) = K(T)\,(\rho\,\alpha). \tag{34}$$

The source term is modeled as described in the one-dimensional case in section 5.3.1.

Numerical convergence study of discontinuous solutions. Here, we test the grid convergence study of the proposed scheme [62, 77]. The computational domain is $\Omega = [0,2] \times [0,2]$ and the initial conditions consist of a circular burnt region as

$$(\rho_0, u_0, v_0, p_0, \alpha_0) = \begin{cases} (1,\ 0,\ 0,\ 80,\ 0) & \text{if } x^2 + y^2 \leq 0.36, \\ (1,\ 0,\ 0,\ 10^{-9},\ 1) & \text{otherwise,} \end{cases} \tag{35}$$

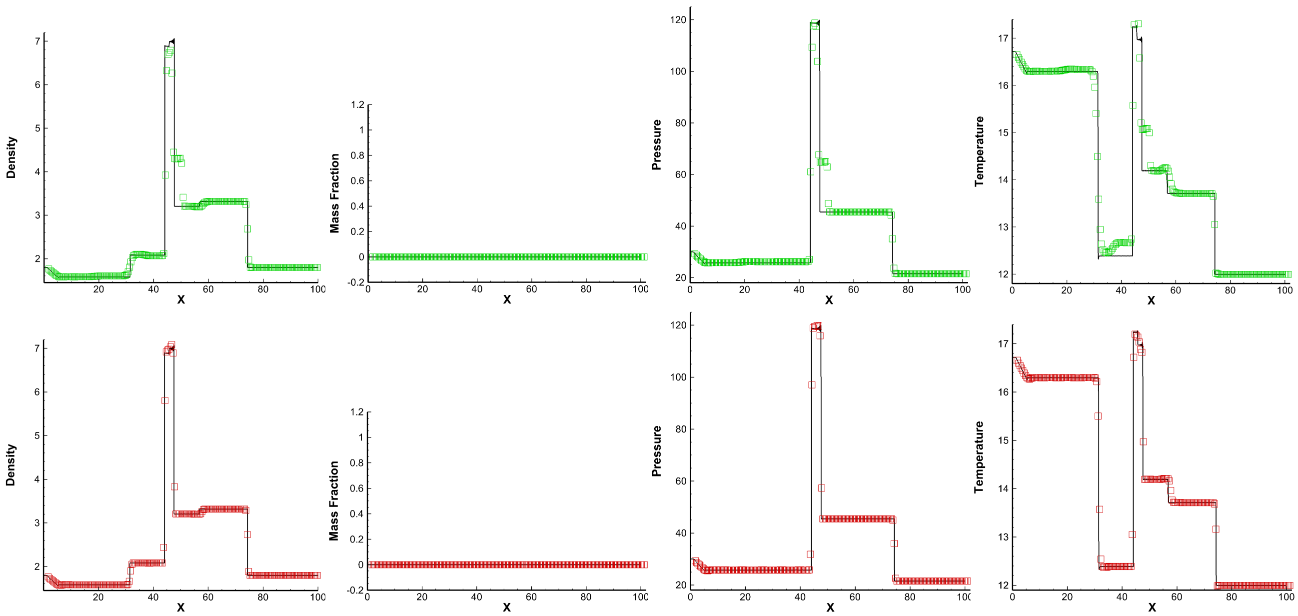

Figure 12: Numerical results for density, mass fraction, pressure and temperature of collision of two detonations — After collision at time $t_2 = 6$ – Top: WENO-JS scheme (green symbols); Bottom: Present BVD-MOOD scheme (red symbols).

with reflective boundary conditions on the left and on the bottom and outflow on top and right ones. The final time is $t_{\text{final}} = 0.2$ and the parameters are $\gamma = 1.2$, $q = 50$, $T_{ign} = 50$, $K_0 = 2566.4$. The numerical simulations are performed over a uniform mesh made of $N_x \times N_y$ cells with $N_x = N_y = 160$ and $N_x = N_y = 320$ respectively. In figure 13 we illustrate the density and pressure in color maps for the finer mesh. Furthermore, we observe that the results obtained by the present scheme for the two meshes show a good convergence in this grid-refinement test, and the results are comparable to those in [62, 77]. Even though the value of density is low, the present scheme can simulate the test without any blow-up or code crash.

Detonation-diffraction problems. In this subsection, some detonation-diffraction problems are simulated, see [76, 62, 42]. Physically, the test consists of the detonation-diffraction of a shock wave emerging at a sharp convex corner with 90^o angle or passing around an obstacle with 180^o angle. There exists no general theory to completely analyze this situation. However, this problem has been extensively numerically studied to understand the flow features produced by detonation-diffraction of a shock wave. It became a popular challenging test case for numerical

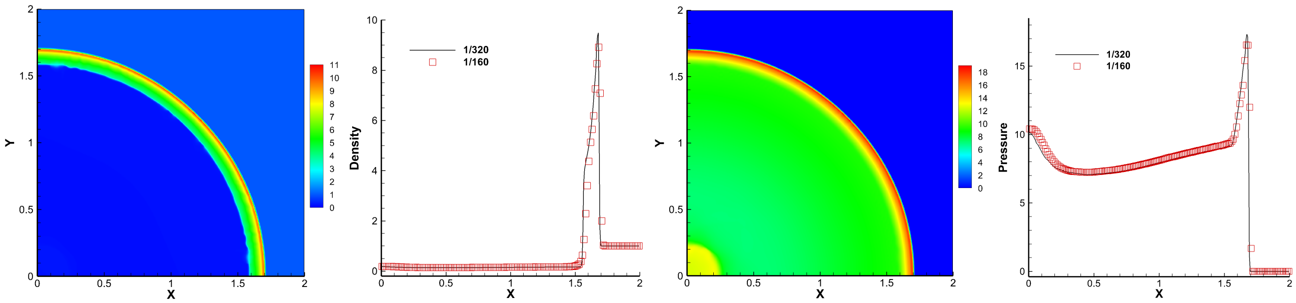

(a) (b) (c) (d)

Figure 13: Numerical results for numerical convergence study – (a) Color map of density; (b) Cut along the line $y = 0.25$ for density; (c) Color map of pressure; (d) Cut along the line $y = 0.25$ for pressure.

methods because the density and pressure drop drastically towards zero, and positivity issues are often encountered. The initial condition is given as

$$(\rho_0, u_0, v_0, E_0, \alpha_0) = \begin{cases} (11,\ 6.18,\ 0,\ 970,\ 1) & \text{if } x < L_s, \\ (1,\ 0,\ 0,\ 55,\ 1) & \text{otherwise,} \end{cases} \tag{36}$$

where L_s is the initial shock location. The parameters of the model are $\gamma = 1.2, q = 50, T_{ign} = 50, K_0 = 2566.4$.

90^o **corner test problem.** The computational domain is the union of $\Omega_1 = [0, 1] \times [2, 5]$ and $\Omega_2 = [1, 5] \times [0, 5]$. A vertical shock is initially located at $L_s = 0.5$. The boundary conditions are reflective everywhere, except that at the left-most boundary $x = 0$ where $(\rho_{\text{in}}, u_{\text{in}}, v_{\text{in}}, E_{\text{in}}, \alpha_{\text{in}}) = (11,\ 6.18,\ 0,\ 970,\ 1)$ is imposed as inflow boundary condition. The final time of the computation is $t_{\text{final}} = 0.6$. The color maps and iso-line contours of density and pressure computed by the present BVD-MOOD scheme with $N_x \times N_y = 400 \times 400$ cells are plotted in figure 14. The complex flow structures generated from the diffraction of the detonation wave at the corner is in adequation with the results from [76, 62, 42]. Moreover, we can observe that the density and pressure drop down to values 0.0077 and 0.00023, respectively, for our simulation.

180^o **corner test problem.** The computational domain is $\Omega = [0, 6] \times [0, 5]$ with a wall type obstacle $A = [0, 1.5] \times [2, 2]$. The initial vertical shock is located at $L_s = 1$. The boundary conditions are reflective ones everywhere, except for the left-most boundary $x = 0$ and $y > 2$ where inflow is imposed like previously. The final time of the computation is $t_{\text{final}} = 0.68$. The color maps and iso-line contours for the density and pressure computed by the BVD-MOOD

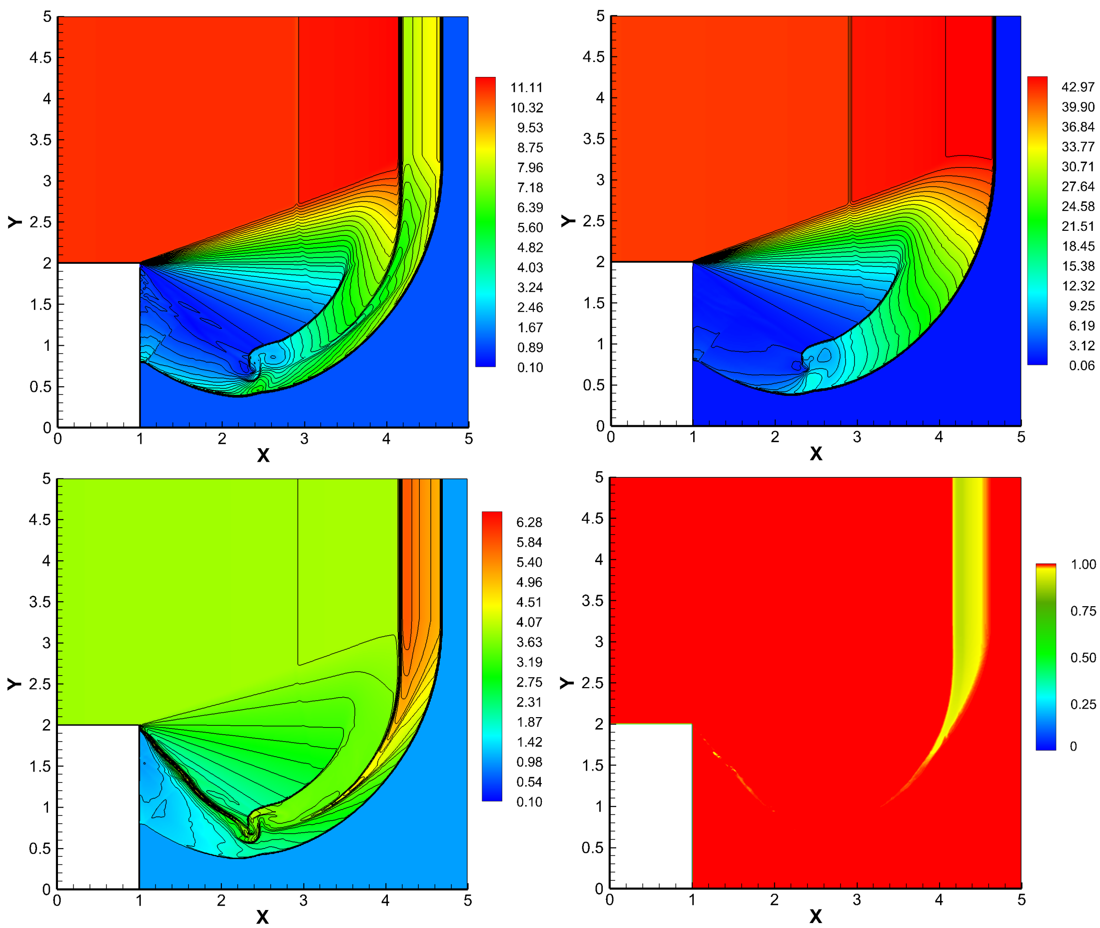

Figure 14: 2D Reactive Euler equations — Diffraction of detonation waves — Numerical results of a 90^o corner test case at time $t_{\text{final}} = 0.6$ with 400×400 mesh cells simulated by the BVD-MOOD scheme – Top-left panel: Density variable; Top-right panel: Pressure variable; Bottom-left panel: Temperature variable; Bottom-right panel: Mass fraction variable.

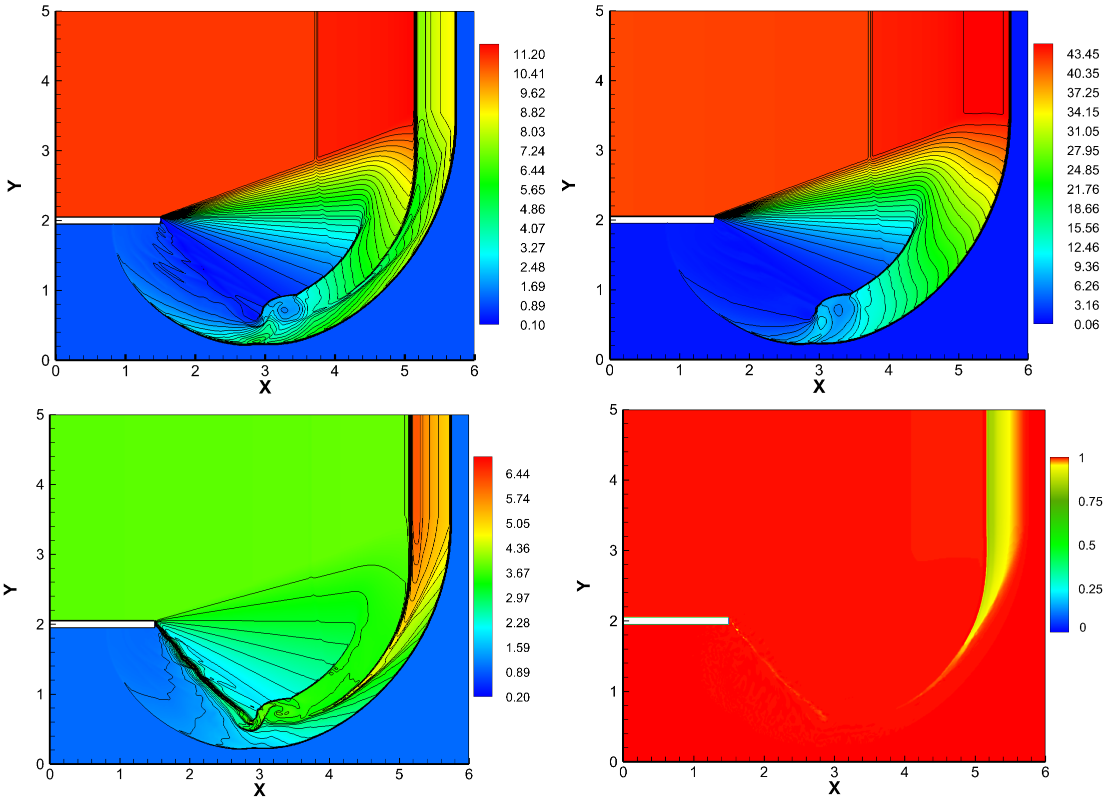

Figure 15: 2D Reactive Euler equations — Diffraction of detonation waves — Numerical results of 180^o corner test case at time $t_{\text{final}} = 0.68$ with 480×400 mesh cells simulated by the BVD-MOOD scheme – Top-left panel: Density variable; Top-right panel: Pressure variable; Bottom-left panel: Temperature variable; Bottom-right panel: Mass fraction variable.

scheme with $N_x \times N_y = 480 \times 400$ cells are plotted in figure 15. Again the main flow structures are well resolved and in good agreement with the ones in [42] without any trouble concerning the positivity preservation or the out-of-bound mass fraction, or, any robustness problem in general.

In our simulations for these two demanding test cases, the MOOD loop appropriately handles the occurrence of negative density/pressure as well as out-of-bound mass fraction, which are cured by the ultimate use of first-order Godunov scheme when and where required.

Multiple obstacles problem. As the last test case, we simulate the detonation wave passing multiple rectangular obstacles [62, 42] which is a even more challenging test case for the positivity preservation property. The main reason is that spurious negative density and/or pressure may occur below and on any of the sharp corners. The computational domain is $\Omega = [0, 8.3] \times [0, 10]$ with the first and second obstacle located at $A_1 = [1.3, 3.3] \times [0, 2.6]$ and $A_2 = [5.1, 8.3] \times [0, 4.3]$, respectively. The boundary conditions are reflective everywhere including the surface of obstacles. The related model parameters are set $\gamma = 1.2$, $q_0 = 50$, $T_{ign} = 20$, $K_0 = 2410.2$. The initial condition is

$$(\rho_0, u_0, v_0, E_0, \alpha_0) = \begin{cases} (7,\ 0,\ 0,\ 200,\ 0) & \text{if } x^2 + y^2 \leq 0.36, \\ (1,\ 0,\ 0,\ 55,\ 1) & \text{otherwise}, \end{cases} \tag{37}$$

which corresponds to a cylindrical detonation wave separating the burnt from the un-burnt gas. The final time is set to $t_{\text{final}} = 1.4$. The numerical results are performed over the uniform mesh made of $N_x \times N_y = 332 \times 400$ cells. The 30 colored contours of density and pressure are presented in figure 16, which fit well with those in [62, 42]. Again, the BVD-MOOD scheme maintains the positivity of the physical variables (density, pressure) and the in-bound property of the mass fraction α.

6. Conclusion

In this paper we have presented a solution properties preserving reconstruction method called multi-stage BVD-MOOD scheme which solves the compressible Euler equations supplemented with three types of source terms. Different from the classical high order schemes based on a *a priori* limited polynomial reconstructions, the present scheme employs limiter-free mixed reconstructions. More precisely the algorithm relies on the Boundary Variation Diminishing (BVD) algorithm to choose between (1) a 4^{th} order unlimited polynomial interpolation for smooth profiles, (2) non-linear monotone THINC (hyperbolic tangent) functions of different smoothness to add dissipation and suppress spurious oscillations, (3) a sharp non-linear THINC function to deal with discontinuity and steep gradients, and (4) no reconstruction (i.e piecewise-constant leading to the 1^{st} order Godunov FV scheme) for extreme situations as the last resort.

The BVD strategy consists in selecting the reconstruction in one cell which is producing the smallest jumps at the cell boundaries because the numerical dissipation scales with those jumps. The BVD algorithm automatically selects the highest possible polynomial interpolation

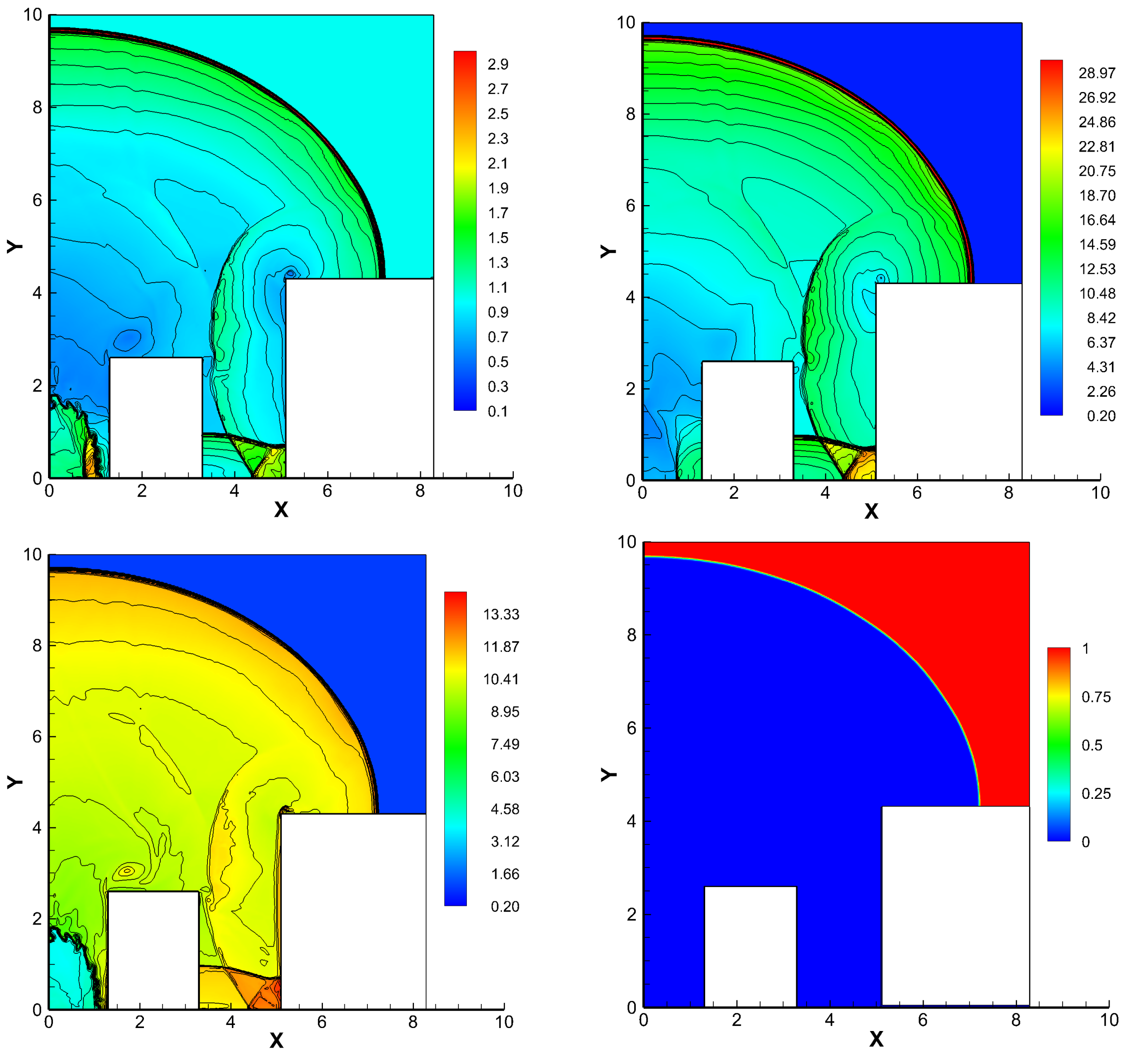

Figure 16: 2D Reactive Euler equations — Diffraction of detonation waves — Numerical results of multiple obstacles problem at time $t_{\text{final}} = 1.4$ with 332×400 mesh cells simulated by the BVD-MOOD scheme – Top-left panel: Density; Top-right panel: Pressure; Bottom-left panel: Temperature; Bottom-right panel: Mass fraction.

$\mathbb{P}_4$ for smooth solutions, the THINC reconstruction with a mild steepness on non-smooth area, which provides an oscillation-free solution (similar to TVD-MUSCL), and the step-like THINC shape to capture sharply the genuine discontinuous solution (contact, material interface, shock). Furthermore, the scheme is supplemented with an *a posteriori* MOOD loop to ensure that the numerical solution remains in its admissible set. If the candidate solution at time t^{n+1} does not satisfy the Physical Admissible Detection (PAD) criterion, then the solution is locally recomputed with a 1^{st} order FV scheme. The *a posteriori* MOOD loop cures for instance the lack of positivity for density or internal energy, the in-bound property of mass fraction and the computer un-representable floating points `Nan, Inf`.

In our approach, among several reconstructions, the scheme is able to choose the most appropriate one according to some goodness criteria; the *a priori* BVD (least dissipative reconstruction), and, an *a posteriori* MOOD (robustness and fail-safe).

Based on the numerical experiments of benchmark test problems, it is demonstrated that the present scheme can sharply capture the discontinuity, material interfaces, contacts, shocks and detonation fronts in both 1D and 2D. Moreover due to the small but sufficient numerical dissipation, the small-scale structures are well represented, simultaneously with the prevention of the occurrence of spurious oscillations. The *a posteriori* detection loop renders the scheme extremely robust to positivity issues. The comparison with the state of the art of high accurate numerical schemes such as WENO-JS is generally in favor of our approach. Recall that our approach is 'limiter-free' in the sense that the mechanism of dissipation is brought by the appropriate choice of the type of reconstruction (polynomial, smooth THINC, sharp THINC, piecewise constant). In the future we plan to extend the approach to three dimensions and unstructured grids to handle more complex geometrical configurations. Moreover the application of our scheme to more complex PDEs such as multiphase flows is expected.

Acknowledgments

This work was supported in part by the fund from JSPS (Japan Society for the Promotion of Science) under Grant Nos. 17K18838, 18H01366 and 19H05613.

In memoriam

This paper is dedicated to the memory of Dr. Douglas Nelson Woods (*January 11$^{\text{th}}$ 1985 - †September 11$^{\text{th}}$ 2019), promising young scientist and post-doctoral research fellow at Los Alamos National Laboratory. Our thoughts and wishes go to his wife Jessica, to his parents Susan and Tom, to his sister Rebecca and to his brother Chris, whom he left behind.

References

[1] F. Acker, R. Borges, and B. Costa. An improved WENO-Z scheme. *J. Comput. Phys.*, 313:726–753, 2016.

[2] W. Bao and S. Jin. The random projection method for stiff detonation capturing. *SIAM J. Sci. Comput.*, 23(3):1000–1026, 2001.

[3] M. Ben-Artzi. The generalized Riemann problem for reactive flows. *J. Comput. Phys.*, 81(1):70 – 101, 1989.

[4] F. Blachère and R. Turpault. An admissibility and asymptotic preserving scheme for systems of conservation laws with source term on 2d unstructured meshes with high-order MOOD reconstruction. *Comput Method Appl M*, 317:836 – 867, 2017.

[5] J.P. Boris and D.L. Book. Flux-corrected transport. I. SHASTA, a fluid transport algorithm that works. *J. Comput. Phys.*, 11(1):38 – 69, 1973.

[6] W. Boscheri, M. Dumbser, R. Loubère, and P.H. Maire. A second-order cell-centered Lagrangian ADER-MOOD finite volume scheme on multidimensional unstructured meshes for hydrodynamics. *J. Comput. Phys.*, 358:103 – 129, 2018.

[7] W. Boscheri, R. Loubère, and M. Dumbser. Direct arbitrary-Lagrangian-Eulerian ADER-MOOD finite volume schemes for multidimensional hyperbolic conservation laws. *J. Comput. Phys.*, 292:56 – 87, 2015.

[8] Walter Boscheri and Michael Dumbser. Arbitrary-lagrangian–eulerian discontinuous galerkin schemes with a posteriori subcell finite volume limiting on moving unstructured meshes. *Journal of Computational Physics*, 346:449 – 479, 2017.

[9] A.J. Chorin. Random choice methods with applications to reacting gas flow. *J. Comput. Phys.*, 25(3):253 – 272, 1977.

[10] S. Clain, S. Diot, and R. Loubère. A high-order finite volume method for systems of conservation laws - Multi-dimensional Optimal Order Detection (MOOD). *J. Comput. Phys.*, 230:4028–4050, 2011.

[11] S. Clain and J. Figueiredo. The MOOD method for the non-conservative shallow-water system. *Comput Fluids*, 145:99 – 128, 2017.

[12] P. Colella, A. Majda, and V. Roytburd. Theoretical and numerical structure for reacting shock waves. *SIAM Journal on Scientific and Statistical Computing*, 7(4):1059–1080, 1986.

[13] P. Colella and P. Woodward. The piecewise parabolic method (ppm) for gas-dynamical simulations. *J. Comput. Phys.*, 54(1):174 – 201, 1984.

[14] X. Deng, S. Inaba, B. Xie, K.M. Shyue, and F. Xiao. High fidelity discontinuity-resolving reconstruction for compressible multiphase flows with moving interfaces. *J. Comput. Phys.*, 371:945 – 966, 2018.

[15] X. Deng, Y. Shimizu, and F. Xiao. Constructing high-order discontinuity-capturing schemes with linear-weight polynomials and boundary variation diminishing algorithm. *arXiv preprint*, arXiv:1811.08316, 2018.

[16] X. Deng, Y. Shimizu, and F. Xiao. A fifth-order shock capturing scheme with two-stage boundary variation diminishing algorithm. *J. Comput. Phys.*, 386:323–349, 2019.

[17] X. Deng, B. Xie, R. Loubère, Y. Shimizu, and F. Xiao. Limiter-free discontinuity-capturing scheme for compressible gas dynamics with reactive fronts. *Comput Fluids*, 171:1–14, 2018.

[18] X. Deng, B. Xie, F. Xiao, and H. Teng. New accurate and efficient method for stiff detonation capturing. *AIAA Journal*, 56(10):4024–4038, 2018.

[19] S. Diot, S. Clain, and R. Loubère. Improved detection criteria for the Multi-dimensional Optimal Order Detection (MOOD) on unstructured meshes with very high-order polynomials. *Comput Fluids*, 64:43–63, 2012.

[20] M. Dumbser and R. Loubère. A simple robust and accurate a posteriori sub-cell finite volume limiter for the discontinuous Galerkin method on unstructured meshes. *J. Comput. Phys.*, 319:163 – 199, 2016.

[21] M. Dumbser, O. Zanotti, R. Loubère, and S. Diot. A posteriori subcell limiting of the discontinuous Galerkin finite element method for hyperbolic conservation laws. *J. Comput. Phys.*, 278:47–75, 2014.

[22] Michael Dumbser, Ilya Peshkov, Evgeniy Romenski, and Olindo Zanotti. High order ader schemes for a unified first order hyperbolic formulation of newtonian continuum mechanics coupled with electro-dynamics. *Journal of Computational Physics*, 348:298 – 342, 2017.

[23] C. Escalante, M. Dumbser, and M.J. Castro. An efficient hyperbolic relaxation system for dispersive non-hydrostatic water waves and its solution with high order discontinuous galerkin schemes. *Journal of Computational Physics*, 394:385 – 416, 2019.

[24] F. Fambri, M. Dumbser, S. Köppel, L. Rezzolla, and O. Zanotti. ADER discontinuous Galerkin schemes for general-relativistic ideal magnetohydrodynamics. *Mon. Not. R. Astron. Soc.*, 477(4):4543–4564, 03 2018.

[25] P. Fan, Y. Shen, B. Tian, and C. Yang. A new smoothness indicator for improving the weighted essentially non-oscillatory scheme. *J. Comput. Phys.*, 269:329 – 354, 2014.

[26] L. Fu, X.Y. Hu, and N.A. Adams. A family of high-order targeted ENO schemes for compressible-fluid simulations. *J. Comput. Phys.*, 305:333 – 359, 2016.

[27] Elena Gaburro, Walter Boscheri, Simone Chiocchetti, Christian Klingenberg, Volker Springel, and Michael Dumbser. High order direct arbitrary-lagrangian-eulerian schemes on moving voronoi meshes with topology changes. *Journal of Computational Physics*, 407:109167, 2020.

[28] C.L. Gardner, J. Glimm, O. McBryan, R. Menikoff, D.H. Sharp, and Q. Zhang. The dynamics of bubble growth for Rayleigh-Taylor unstable interfaces. *Phys. Fluids*, 31(3):447–465, 1988.

[29] S. K. Godunov. A difference scheme for numerical solution of discontinuous solution of hydrodynamic equations. *Mat. Sb.*, 47(3):271 – 306, 1959.

[30] S. Gottlieb. On high order strong stability preserving Runge-Kutta and multi step time discretizations. *J. Sci. Comput.*, 25:105–128, 2005.

[31] A. Harten. High resolution schemes for hyperbolic conservation laws. *J. Comput. Phys.*, 49(3):357 – 393, 1983.

[32] C. Helzel, R.J. Leveque, and G. Warnecke. A modified fractional step method for the accurate approximation of detonation waves. *SIAM J. Sci. Comput.*, 22(4):1489–1510, 2000.

[33] H.T. Huynh. Schemes and constraints for advection time stepping method with flux reconstruction view project. *Art. Lec. Notes Phys.*, 1997.

[34] G.S. Jiang and C.W. Shu. Efficient implementation of weighted ENO schemes. *J. Comput. Phys.*, 126:202–228, 1996.

[35] Z.H. Jiang, X. Deng, F. Xiao, C. Yan, and J. Yu. A high order interpolation scheme of finite volume method for compressible flow on curvilinear grids. *Commun. Comput. Phys. (in press)*, 2020.

[36] Z.H. Jiang, C. Yan, and J. Yu. Efficient methods with higher order interpolation and MOOD strategy for compressible turbulence simulations. *J. Comput. Phys.*, 371:528 – 550, 2018.

[37] C.Y. Jung and T.B. Nguyen. Fine structures for the solutions of the two-dimensional Riemann problems by high-order WENO schemes. *Adv. Comput. Math.*, 44(1):147–174, Feb 2018.

[38] A. Kurganov and E. Tadmor. Solution of two-dimensional Riemann problems for gas dynamics without Riemann problem solvers. *Numer Meth Part D E*, 18:584–608, 2002.

[39] P.D. Lax and X.D. Liu. Solution of two-dimensional Riemann problems of gas dynamics by positive schemes. *SIAM J. Sci. Comput.*, 19(2):319–340, 1998.

[40] B. Van Leer. Towards the ultimate conservative difference scheme. iv. a new approach to numerical convection. *J. Comput. Phys.*, 23(3):276 – 299, 1977.

[41] B. Van Leer. Towards the ultimate conservative difference scheme. v. a second-order sequel to Godunov's method. *J. Comput. Phys.*, 32(1):101 – 136, 1979.

[42] P. Li, W.S. Don, C. Wang, and Z. Gao. High order positivity- and bound-preserving hybrid compact-WENO finite difference scheme for the compressible Euler equations. *J. Sci. Comput.*, 74(2):640–666, Feb 2018.

[43] Q. Li, P. Liu, and H. Zhang. Piecewise polynomial mapping method and corresponding WENO scheme with improved resolution. *Commun. Computat. Phys.*, 18(5):1417–1444, 2015.

[44] T. Linde and P.L. Roe. Robust Euler codes. *in: Thirteenth Computational Fluid Dynamics Conference*, pages AIAA–97–2098, 1997.

[45] C. Lohmann and D. Kuzmin. Synchronized flux limiting for gas dynamics variables. *J. Comput. Phys.*, 326:973 – 990, 2016.

[46] Y.X. Ren, M. Liu, and H. Zhang. Efficient implementation of weighted ENO schemes. *J. Comput. Phys.*, 192:365–386, 2003.

[47] C.W. Schulz-Rinne. Classification of the Riemann problem for two-dimensional gas dynamics. *SIAM J. Math. Anal.*, 24:76–88, 1993.

[48] Z. Shen, W. Yan, and G. Yuan. A robust HLLC-type Riemann solver for strong shock. *J. Comput. Phys.*, 309:185 – 206, 2016.

[49] C.W. Shu and S. Osher. Efficient implementation of essentially non-oscillatory shock-capturing schemes. *J. Comput. Phys.*, 77:439–471, 1988.

[50] C.W. Shu and S. Osher. Efficient implementation of essentially non-oscillatory shock-capturing schemes, ii. *J. Comput. Phys.*, 83:32–78, 1989.

[51] K.M. Shyue and F. Xiao. An Eulerian interface sharpening algorithm for compressible two-phase flow: The algebraic THINC approach. *J. Comput. Phys.*, 268:326–354, 2014.

[52] G. Strang. On the construction and comparison of difference schemes. *SIAM J. Numer. Anal.*, 5(3):506–517, 1968.

[53] Z. Sun, S. Inaba, and F. Xiao. Boundary variation diminishing (BVD) reconstruction: A new approach to improve Godunov schemes. *J. Comput. Phys.*, 322:309–325, 2016.

[54] P.K. Sweby. High resolution schemes using flux limiters for hyperbolic conservation laws. *J. Comput. Phys.*, 21(5):995 – 1011, 1984.

[55] S. Tann, X. Deng, Y. Shimizu, R. Loubère, and F. Xiao. Solution property preserving reconstruction for finite volume scheme: a boundary variation diminishing+multidimensional optimal order detection framework. *Int. J. Numer. Methods Fluids*, pages 1–32, 2019.

[56] Maurizio Tavelli and Michael Dumbser. A pressure-based semi-implicit space–time discontinuous galerkin method on staggered unstructured meshes for the solution of the compressible navier–stokes equations at all mach numbers. *Journal of Computational Physics*, 341:341 – 376, 2017.

[57] Maurizio Tavelli, Michael Dumbser, Dominic Etienne Charrier, Leonhard Rannabauer, Tobias Weinzierl, and Michael Bader. A simple diffuse interface approach on adaptive cartesian grids for the linear elastic wave equations with complex topography. *Journal of Computational Physics*, 386:158 – 189, 2019.

[58] V.A. Titarev and E.F. Toro. ADER schemes for three-dimensional non-linear hyperbolic systems. *J. Comput. Phys.*, 204(2):715 – 736, 2005.

[59] E.F. Toro. *Riemann solvers and numerical methods for fluid dynamics: a practical introduction.* Springer Verlag, 2009.

[60] L. Tosatto and L. Vigevano. Numerical solution of under-resolved detonations. *J. Comput. Phys.*, 227(4):2317 – 2343, 2008.

[61] R. Turpault and T. Nguyen-Bui. A high order MOOD method for compressible Navier-Stokes equations: application to hypersonic viscous flows. *Progress in Computational Fluid Dynamics, an International Journal*, 19(6):337–345, 2019.

[62] C. Wang, X. Zhang, C.W. Shu, and J. Ning. Robust high order discontinuous Galerkin schemes for two-dimensional gaseous detonations. *J. Comput. Phys.*, 231(2):653 – 665, 2012.

[63] W. Wang, C.W. Shu, H.C. Yee, and B. Sjögreen. High order finite difference methods with subcell resolution for advection equations with stiff source terms. *J. Comput. Phys.*, 231(1):190 – 214, 2012.

[64] L. White and A. Adcroft. A high-order finite volume remapping scheme for nonuniform grids: The piecewise quartic method (PQM). *J. Comput. Phys.*, 227(15):7394–7422, 2008.

[65] P. Woodward and P. Colella. The numerical simulation of two-dimensional fluid flow with strong shocks. *J. Comput. Phys.*, 54:115–173, 1984.

[66] F. Xiao, K. Honma, and T. Kono. A simple algebraic interface capturing scheme using hyperbolic tangent function. *Int. J. Numer. Methods Fluids*, 48:1023–1040, 2005.

[67] F. Xiao, S. Ii, and C. Chen. Revisit to the THINC scheme: A simple algebraic VOF algorithm. *J. Comput. Phys.*, 230:7086–7092, 2011.

[68] Z. Xu and C.W. Shu. Anti-diffusive flux corrections for high order finite difference WENO schemes. *J. Comput. Phys.*, 205(2):458 – 485, 2005.

[69] Z. Xu and X. Zhang. Chapter 4 - bound-preserving high-order schemes. In R. Abgrall and C.W. Shu, editors, *Handbook of Numerical Methods for Hyperbolic Problems*, volume 18 of *Handbook of Numerical Analysis*, pages 81 – 102. Elsevier, 2017.

[70] Y.N. Young, H. Tufo, A. Dubey, and R. Rosner. On the miscible Rayleigh-Taylor instability: two and three dimensions. *J. Fluid Mech.*, 447:377–408, 2001.

[71] S.T. Zalesak. Fully multidimensional flux-corrected transport algorithms for fluids. *J. Comput. Phys.*, 31(3):335 – 362, 1979.

[72] O. Zanotti, F. Fambri, M. Dumbser, and A. Hidalgo. Space–time adaptive ADER discontinuous Galerkin finite element schemes with a posteriori sub-cell finite volume limiting. *Comput Fluids*, 118:204 – 224, 2015.

[73] X. Zhang and C.W. Shu. On positivity-preserving high order discontinuous Galerkin schemes for compressible Euler equations on rectangular meshes. *J. Comput. Phys.*, 229:8918–8934, 2010.

[74] X. Zhang and C.W. Shu. Maximum-principle-satisfying and positivity-preserving high-order schemes for conservation laws: survey and new developments. *P. Roy. Soc. A-Math. Phy.*, 467(2134):2752–2776, 2011.

[75] X. Zhang and C.W. Shu. Positivity-preserving high order discontinuous Galerkin schemes for compressible Euler equations with source terms. *J. Comput. Phys.*, 230(4):1238–1248, 2011.

[76] X. Zhang and C.W. Shu. Positivity-preserving high order finite difference WENO schemes for compressible Euler equations. *J. Comput. Phys.*, 231(5):2245 – 2258, 2012.

[77] H. Zhu and Z. Gao. An h-adaptive RKDG method for two-dimensional detonation wave simulations. *E Asian J Appl Math*, 9(1):165–184, 2019.